FRERES MENTOURI UNIVERSITY
CONSTANTINE 1 -ALGERIA

Journal of Sciences & Technology

Semestrial Journal of Freres Mentouri University, Constantine, Algeria

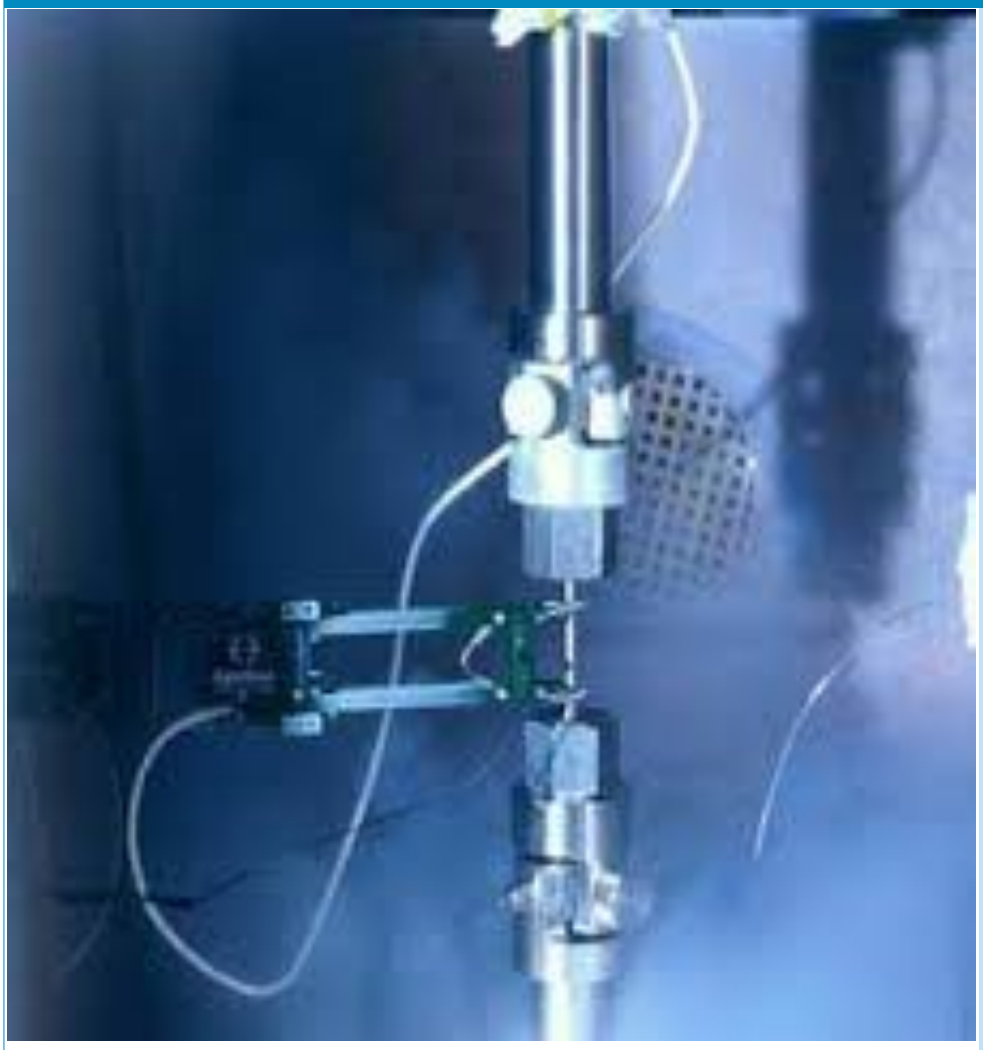

VOLUME 03 - ISSUE 02— DECEMBER 2018

EISSN: ….-….

Freres Mentouri
University Constantine

Ain El-Bey Road
Constantine 25000
Algeria

Phone.Fax: 213 (0) 31. 81. 12.78
Email: revues@umc.edu.dz
Website :http://revue.umc.edu.dz

Journal of Sciences & Technology

Volume 3 N° 2 December 2018

Semestrial Journal of Freres Mentouri Constantine 1 University, Algeria

An article proposed for publication should not be submitted at the same time to another journal.

Manuscripts (original and two copies) should be sent to the following address:

Vice-Rectorate in charge of Post-Graduation and Scientific Research

Direction of Publications and Scientific Animation (15th floor)

Constantine 1 University , Aïn-El-Bey Road, 25000 Constantine, ALGERIA.

Tél./Fax: 213 (0) 31.81.12.78

e-mail: revues@umc.edu.dz

Constantine1 University

Journal of Sciences & Technology

Volume 3 N° 2 – December 2018

SCIENTIFIC COMMITTEE

INSTRUCTIONS TO AUTHORS

I- Overview

The journal Human Sciences publishes in three languages: Arabic, French and English. Two abstracts must be provided, one in the language of the article, the other in Arabic if the article is written in another language, or in French (or English) if the article is written in Arabic. Abstracts must not exceed 150 words. Unpublished articles are not returned to their authors.

II- Manuscrips

The articles submitted for publication (three copies) must not exceed 20 typewritten pages (tables, figures, graphs, bibliography, ... included) with a large margin to the left (3 cm), printed on 21 x 29 paper , 7 cm (A4) with interligne of good readability. Some flexibility is allowed to authors, but they should organize the text clearly in sections such as: Introduction, Experimental Details, Results, Discussion and Conclusion. The longer articles will be published by part in successive issues, each part being determined by the authors. Authors are kindly requested to accompany the summary of their articles with the most complete possible keywords.

In order to save time and respect deadlines for publication, it is recommended that authors take care of the complete capture of their article on a computer, and send it to the journal, after they have been informed. acceptance for publication, in the form of files on CD.ROM, which will be copied by the service.

However, since the final formatting of the article is done by P.A.O. (Computer Aided Publication), the authors are asked to avoid any formatting of their text. It will be necessary to avoid stylizing it.

III- Bibliography

The bibliographic references quoted in the text must include only the reference number in square brackets (ex .: [5]). If the name of the author appears in the text, it must be followed by the reference number. When the reference contains more than two authors, only the first is cited, followed by "and al".

For articles, the complete reference includes the names of the authors followed by the initials of their first names, the title of the article, the title of the periodical (in conformity with the abbreviations allowed), the volume, the number of the periodical, the year of publication and the relevant pages.

For the works, the reference must include the names of the authors followed by the initials of their first names, the complete title of the work, the volume, the volume, the first and the last page relating to the results discussed, the number of the edition if there are several, the name of the publisher, the place and the year of edition.

For scientific meetings (congresses, proceedings, ...), the reference includes the names of the authors followed by the initials of their first names, the title of the communication, the identification of the meeting, the place, the period and the pages concerned.

IV- Iconography

Tables, boards, charts, maps, photographs, etc. must be provided separately, inset. They must be presented on white sheets of A4 format, individually or in groups, and have underneath the words "table" or "figure" assigned a number.

The illustrations and figures must be clear, professionally made and adequate for reproduction: a 50% reduction, if any, must lead to a suitable size and thickness of characters for good readability. Moreover, for computer-generated figures, in order to maximize contrast, the use of a laser or inkjet printer is essential.

Legends assigned their numbers must be grouped in a separate page.

The final presentation of the article will be left to the discretion of the Editorial Board.

Journal of Sciences & Technology
Volume 3 N° 2– December 2018

SUMMARY

SUMMARY

Journal of Sciences & Technology
Volume 3 N° 2– December 2018

MODELING OF THE SOLUBILITY IN SUPERCRITICAL CARBON DIOXIDE OF SOME SOLID SOLUTE ISOMERS USING THE EXPANDED LIQUID THEORY.

Submited on 12/08/2016 – Accepted on 24/12/2016

Abstract

One of the most important research fields of supercritical fluid technology is the solubility of solids in supercritical fluids. Solubility data is fundamental to the development of new supercritical applications as biodiesel production and refrigeration, and the enhancement of existing applications including environmental pollution, extraction and purification of pharmaceuticals, food and natural products, and natural gas industry. Hence, the ability to correlate and predict the solubility of solids in supercritical fluids is of utmost importance. In this work, we propose to correlate and predict the solubility in supercritical CO2 of disubstituted aromatic isomers of hydroxybenzoic acid with a new model based on the expanded liquid theory, in which the solid–fluid equilibrium is modeled using the local composition model of UNIQUAC in which the interaction parameters are related to the solvent reduced density with an empiric exponential form equations. The experimental solubility data of o-hydroxybenzoic acid, p-hydroxybenzoic acid, m-hydroxybenzoic acid and mixed isomers (m-hydroxybenzoic acid+p-hydroxybenzoic acid) are used for evaluating the correlation and prediction capabilities of this new model. The results obtained using the proposed model show good agreement with the experimental data used.

Keywords: *supercritical fluid, aromatic isomers, correlation, prediction, solubility.*

L NASRI [1]
Z BENSETITI [2]
S BENSAAD [3]

1 Department of Industrial Chemistry, Frères Mentouri University, Algeria.

2 Unisignal Inc., Brossard, Quebec, Canada.

3 Department of Chemistry, Frères Mentouri University, Algeria.

I- INTRODUCTION

During the past few years, widespread attention has been focused on supercritical fluids due to their potential application in extraction processes in food processing, pharmaceutical and petroleum industries, etc. The main advantages of supercritical fluid extraction over conventional extraction methods include increased speed, easy solvent separation and better recovery, and reduction in both solvent usage and solvent waste generation. The most widely used supercritical fluid is carbon dioxide because it is nontoxic, nonflammable and relatively inexpensive, and possesses reasonable critical properties (t_C=30°C and P_C=72atm) as well as a high solvent power for a wide range of nonpolar and intermediately polar organic compounds. The solubility of a solute in a supercritical fluid is perhaps the most important thermophysical property that must be determined and modeled for an efficient design of any extraction procedure based on supercritical solvents. The determination of solubilities of a wide variety of solids and liquids of low volatility in supercritical carbon dioxide has received considerable attention in recent years. However, despite the vital importance of the solubility data of isomeric compounds from chemical, biochemical, pharmaceutical and industrial points of view, there is still a lack of fundamental solubility and mass-transfer data available in the literature to facilitate the development of commercial-scale processes. Since the experimental determination of the solubilities of various solutes in supercritical fluids at each operating condition is tedious, time-consuming and not reported in literatures, there is a considerable interest in mathematical models that can accurately predict the solubilities of solid solutes in supercritical fluids [1].

Aromatic isomers serve as raw materials for a wide variety of chemical, pharmaceutical, and polymer products; in some cases the individual isomers are difficult to obtain in pure form, and frequently the separation involves an *ortho-para* pair [2] because in most cases the solute-solute interactions lead to an enhancement in the solubilities of components relative to their respective binary systems [3]. As a consequence, there is now a greater need to understand the solubility behaviour of such systems. Therefore it is essential to have a model that not only can accurately correlate but also predict phase equilibrium properties.

Some of the models that have been used for correlating solubility data can be classified in two classes, equations of state based models (EOS) [4] and empirical models [5]. EOS based models require the prior knowledge of a certain number of parameters such as the critical properties (temperature and pressure), acentric factor and the sublimation pressure of the solid solute. These parameters are not available and are often calculated using group contribution methods, which could lead to solubility error prediction. Due to the lack of information on these properties, empirical models are used for the correlation of experimental solubility data. These models are known as density-based models and consist of equations that contain constants that are empirically adjusted for each compound. Although simple, these models rely much on the knowledge

of the thermodynamic behaviour of the supercritical solvent rather than of the solute, and are mostly capable of correlating rather than predicting the solubility. They are used for quantitative determination of the solute solubility in supercritical phase at equilibrium, and do not provide qualitative information about the solute-solvent interaction.

In this work we will test the methodology previously used [6] that correlates and predicts the solubility of solids in supercritical carbon dioxide based on the expanded liquid model theory [7, 8]. This theory does not require the knowledge of the solute critical properties and sublimation pressure.

In this case the supercritical phase is considered as an *expanded liquid* and is modeled using excess Gibbs energy models such as Margules, Van Laar, and local composition based models i.e. Wilson, NRTL and UNIQUAC. In this study we focus on the use of the UNIQUAC model that has been widely used in modeling vapour-liquid and liquid-liquid equilibrium data. This model does not only take the size and nature of the molecules into consideration, but also accounts for the strength of solute-solvent intermolecular forces. And because the primary concentration variable is the surface fraction rather than mole fraction, the UNIQUAC model is applicable to solutions containing small or large molecules, including polymers.

2. MODEL DEVELOPMENT

The supercritical phase is considered as an expanded liquid phase in equilibrium with the solid phase. The solvent solubility in the solid phase is considered to be negligibly small to consider the solid fugacity to be that of the pure solid. To estimate the solid solubility in the supercritical phase, the knowledge of the activity coefficients are required. These coefficients are determined from the knowledge of the component fugacities, thus when the equilibrium of the pure solid and the supercritical phase is reached, we have:

$$f_2^{s} = f_2^{SCF} = f_2^{L} \tag{1}$$

f_2^{s} is the fugacity of the solute in the solid phase considered as pure solid and equal to f_2^{os}, f_2^{L} is the fugacity of the solid solute in the supercritical phase and is equal to:

$$f_2^{L} = \gamma_2 y_2 f_2^{oL} \tag{2}$$

Equation (1) could be written as follows:

$$f_2^{os} = \gamma_2 y_2 f_2^{oL} \tag{3}$$

Where γ_2, y_2 and f_2^{oL} are the activity coefficient, the solid solubility represented in mole fraction and the fugacity of the pure solid solute in the expanded liquid phase respectively. According to Prausnitz *et al.* [9], we have:

$$\ln\left(\frac{f_2^{os}}{f_2^{ol}}\right) = \frac{-\Delta H_2^{f}}{R}\left(\frac{1}{T}-\frac{1}{T_m}\right) - \frac{\Delta C_p}{RT}\left(\frac{T-T_m}{T}\right) + \frac{\Delta C_p}{R}\ln\left(\frac{T}{T_m}\right) \tag{4}$$

Prausnitz *et al*. [9] stated that to a fair approximation, the heat capacity terms can be neglected. Equations (3) and (4) then combined to yield an expression for the solute solubility:

$$y_2 = \frac{1}{\gamma_2}\exp\left[\frac{-\Delta H_2^{f}}{R}\left(\frac{1}{T}-\frac{1}{T_m}\right)\right] \tag{5}$$

ΔH_2^{f} is the enthalpy of fusion, T_m is the melting point temperature of the solid solute.

Since the solid solubility in the supercritical phase is very small, it can be assumed that the activity coefficient of the solid solute is the one at infinite dilution and that the density of the solution is that of the pure solvent, i.e. CO_2. Thus equation (5) becomes:

$$y_2 = \frac{1}{\gamma_2^{\infty}}\exp\left[\frac{-\Delta H_2^{f}}{R}\left(\frac{1}{T}-\frac{1}{T_m}\right)\right] \tag{6}$$

The activity coefficient of the solid solute at infinite dilution γ_2^{∞} was calculated using the UNIQUAC model which consists of two parts, a combinatorial part $\gamma_2^{C,\infty}$ that attempts to describe the dominant entropic contribution, and a residual part $\gamma_2^{R,\infty}$ that is due primarily to intermolecular forces that are responsible for the enthalpy of mixing. The combinatorial part is determined only by the composition and by the sizes and shapes of the molecules; it requires only pure-component data. The residual part, however, depends also on intermolecular forces; the two adjustable binary parameters a_{12} and a_{21}, therefore, appear only in the residual part [9]:

$$\ln\gamma_2^{\infty} = \ln\gamma_2^{C,\infty} + \ln\gamma_2^{R,\infty} \tag{7}$$

$$\ln\gamma_2^{C,\infty} = 1 - \frac{r_2}{r_1} + \ln\frac{r_2}{r_1} - q_2\frac{z}{2}\left(1 - \frac{r_2 q_1}{r_1 q_2} + \ln\frac{r_2 q_1}{r_1 q_2}\right) \tag{8}$$

Here q and r are the surface area and volume parameters; z is the coordination number that is usually taken equal to 10. The residual part at infinite dilution is given by the following equation [9]:

$$\ln\gamma_2^{R,\infty} = q_2(1 - \ln\tau_{12} - \tau_{21}) \tag{9}$$

Where

$$\tau_{12} = \exp(-\Delta u_{12}/RT) = \exp(-a_{12}/T)$$
$$\tau_{21} = \exp(-\Delta u_{21}/RT) = \exp(-a_{21}/T) \quad (10)$$

Δu_{12} and Δu_{21} are characteristic energies and are related to the interaction parameters a_{12} and a_{21} through equation (10). Finally combining equations (9) and (10) leads to:

$$\ln\gamma_2^{R,\infty} = q_2 \frac{a_{12}}{T} + q_2\left(1 - e^{\frac{-a_{21}}{T}}\right) \quad (11)$$

Equation (11) could be written in reduced form by introducing the reduced temperature, thus we obtain:

$$\ln\gamma_2^{R,\infty} = q_2 \frac{a'_{12}}{T_r} + q_2\left(1 - e^{\frac{-a'_{21}}{Tr}}\right) \quad (12)$$

With

$a'_{12} = \frac{a_{12}}{T_c}$ and $a'_{21} = \frac{a_{21}}{T_c}$, T_c is the solvent critical temperature.

The binary interaction parameters a'_{12} and a'_{21} are related to the energy of interaction between the solid solute and the solvent in the supercritical phase, and cannot be kept constant and specifically at high pressure conditions. Therefore to take into account the pressure and temperature effects, these parameters are assumed to be density dependant and were fitted to the following equations:

$$a'_{12} = \alpha_{12}.\exp(\beta_{12} \cdot \rho_r) \quad (13a)$$

$$a'_{21} = \alpha_{21}.\exp(\beta_{21} \cdot \rho_r) \quad (13b)$$

ρ_r is the reduced density of the solvent equal to ρ/ρ_c where ρ_c is its critical density, α_{12}, β_{12}, α_{21} and β_{21} are the regressed parameters of the model.

3. ISOMERS SOLUBILITY CALCULATION :

The surface area and volume parameters are calculated as the sum of the group volume and area parameters (R and Q) given by the UNIFAC group specifications [9], since the solutes are isomers they have the same functional groups so they have the same surface area and volume parameters (r_2=4.6869 and q_2=3.624). These parameters and properties listed in Table 1, together with those of carbon dioxide listed in Table 2 are used to calculate the combinatorial part of the activity coefficient from equation (8).

In other hand, equation (12) is used to calculate the residual part of the solid solute activity coefficient. Thermodynamic properties of the solid solute listed in Table 1 are used together with equations (7), (8), and (12) to estimate the solubility y_2 using equation (6). The interaction parameters a'_{12} and a'_{21} are then regressed according to equations (13a) and (13b). The regression is based on minimizing the error between the regressed and experimental solubility data. The error is calculated as the *average absolute relative deviation* (AARD) according to equation (14):

$$AARD(\%) = \frac{1}{N}\left|\sum_1^n \frac{y_{2(exp)} - y_{2(regr)}}{y_{2(exp)}}\right| \times 100 \quad (14)$$

Where N is the number of experimental solubility data of each isomer.

Table 1. Isomers fusion properties

Component	T_m(K)	ΔH_2^f(J/mol)	solubility reference
m-hydroxybenzoic acid	476 [10]	36500 [10]	[2],[3]
p-hydroxybenzoic acid	488,1[10]	30990 [10]	[2],[14]
o-hydroxybenzoic acid	432 [11]	19585 [11]	[2],[3], [13],[14]

Table 2. Solvent physical properties

Solvent	T_c(K)	P_c(bar)	ρ_c(mol/cm^3) ×100	r_1	q_1	Ref
CO_2	304.2	73.83	1.063	1.296	1.261	[9],[12]

4. CORRELATION RESULTS

The interaction parameters a_{12} and a_{21} are regressed through the optimization of the adjustable parameters α_{12}, β_{12}, α_{21} and β_{21}. These fitting parameters are evaluated by minimizing the objective function given in equation (14).

The analysis of the model results is done through statistical calculations. Table 3 provides the quantitative results of the regression for the proposed model. The AARD is listed for each isomer and for each temperature together with the adjustable parameters values and the overall absolute deviations.

Each isomer parameters are obtained by fitting them on its own and whole solubility data. The overall deviations values obtained are generally low and so indicate a good correlation capability of the model.

Table 3. Regression results

Component	N	T(K)	α_{12}	β_{12}	α_{21}	β_{21}	AARD (%)
m-hydroxybenzoic acid	16	318	4,24	-0,292	6497,8	-14,5	1,91
		328					8,23
		373					30,1
		overall					**11,32**
o-hydroxybenzoic acid	84	308	2,83	-0,288	2,35	-2,2	8,6
		313					7,48
		318					11,04
		328					5,74
		373					41,95
		overall					**10,37**
p-hydroxybenzoic acid	16	318	4,57	-0,292	6100,3	-14,9	2,28
		328					6,35
		373					30,4
		overall					**10,84**

From table 3 and figure 1 we can see clearly that the greatest values of AARD are noted at high temperatures especially for T=373K. These can be probably attributed to the very important phenomenon occurring in some high-pressure-mixtures and which is the melting point depression [15], [16].

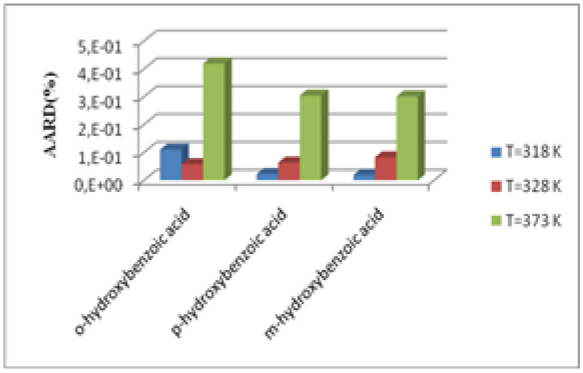

Figure 1. Comparison of the average absolute deviation for the isomers at three different temperatures

Under the influence of high-pressure carbon dioxide, organic solids may undergo melting point depression [17] which lead to the exhibition of fluid-liquid equilibria and so affect the measured solubility data.

Lucien and Foster [14], have mentioned that with their experimental technique for measuring, in all of the systems investigated (pure and mixed) no melting point depression was observed.

However, Krukonis and Kurnik [2] have reported measured solubilities of the hydroxybenzoic acid isomers at very high conditions: T=373K and for pressures greater than 207 bar without indication to the melting point depression phenomenon.

5. PREDICTION RESULTS :

A number of aromatic isomers serve as raw materials for a wide variety of chemical, pharmaceutical, and polymer products and in most cases the individual isomers are difficult to obtain in pure form because binary solubility data present a limited picture of the complex interactions that can occur in the supercritical fluid phase [2]. Consequently, the separation involves a mixture of isomers and frequently an *ortho-para* pair. In this case of mixture solute-solute interactions lead to an enhancement in the solubility of components relative to their respective binary systems [4]. As a consequence, in literature there are several studies on the determination of solubilities of mixed isomers in supercritical carbon dioxide.

In this part, we attempt to predict the solubilities of mixed hydroxybenzoic acid isomers in supercritical carbon dioxide. In this case experimental solubility data provided by Lucien and Foster [3] for an equimolar mixture of the isomers *m*-hydroxybenzoic acid and *p*-hydroxybenzoic acid are used. The solubility data of the too isomers are very small and have an order of 10^{-6}. As a consequence, we can assume that the density of the supercritical phase is that of the pure solvent, and the activity coefficient of each isomer is the one at infinite dilution. In this case the only interaction parameters that are taken into account are those of *m*-hydroxybenzoic-CO_2 and *p*-hydroxybenzoic-CO_2. Therefore predicted solubilities are estimated using equations (6) to (13b) and interaction parameters for both *meta* and *para* isomers listed in table 3 are directly implemented to estimate the solubility of each isomer in the mixture.

Table 4. Prediction results

isomer	N	AARD (%)
m-hydroxybenzoic	12	4,3
p-hydroxybenzoic	12	5,8

The absolute average relative deviation (AARD) obtained are given in table 4. Figures 2a and 2b show a parity plot of the experimental versus predicted solubility data of mixed *m*-hydroxybenzoic and *p*-hydroxybenzoic isomers in supercritical CO_2 for two different temperatures, i.e. 318 and 328K.

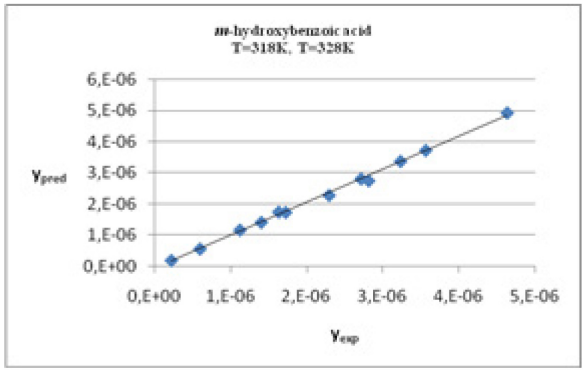

Figure 2 (a)

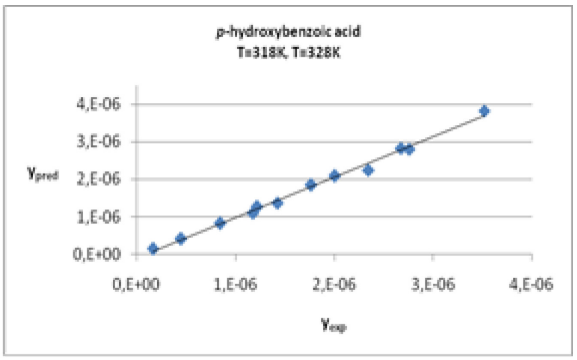

Figure 2 (b)

These figures, and results in table 4 show good agreement between measured solubility data and predicted ones and confirm predictive ability of the proposed model.

6. CONCLUSION

In this work, we have proposed the correlation and prediction of the solubility in supercritical CO_2 of disubstituted aromatic isomers of hydroxybenzoic acid with a new methodology based on the expanded liquid theory, in which the solid–fluid equilibrium is modeled using the local composition model of UNIQUAC. The advantages of this model include the following: it does not require the knowledge of critical properties of solid solutes and does take into account the binary interaction between solid solute and solvent. The results obtained using the proposed model show good agreement with the experimental data of isomers used.

7. REFERENCES

[1] Madras G, Kulkarni C, Modak J. "Modeling the solubilities of fatty acids in supercritical carbon dioxide", *Fluid Phase Equilibria*, 209, pp. 207–213, 2003.

[2] Val J. Krukonis and Ronald T. Kurnik, "Solubility of solid aromatic isomers in carbon dioxide", *Journal of Chemical Engineering Data*, 30, pp. 247-249, 1985.

[3] Frank P. Lucien and Neil R. Foster, "Solubilities of mixed hydroxylbenzoic acid isomers in supercritical carbon dioxide", *Journal of Chemical Engineering Data*, 43, pp. 726-731, 1998.

[4] Foster N.R., Gurdial G.S., Yun J.S.L., Liong K.K., Tilly K.D., Ting S.S.T., Singh H., Lee J.H. *Ind. Eng. Chem. Res*, 30, pp. 1955–1964, 1991.

[5] Chrastil J. "Solubility of Solids and Liquids in Supercritical Gases". *Journal of physical chemistry,* 86, 15, pp. 3016-3021, 1982.

[6] L.Nasri, Z. Bensetiti and Salima Bensaad, "Correlation of the solubility of some organic aromatic pollutants in supercritical carbon dioxide based on the UNIQUAC equation", *Energy Procedia*, 18, pp.1261 – 1270, 2012.

[7] Lee J.W., Min J.M., Bae H.K, "Solubility measurement of disperse dyes in supercritical carbon dioxide", *Journal of Chemical Engineering Data*, 44, pp.684–687, 1999.

[8] Lee J.W., Park M.W., Bae H.K., "Measurement and correlation of dye solubility in supercritical carbon dioxide", *Fluid Phase Equilibria*, 173, 277–284, 2000.

[9] Prausnitz, J. M.; Lichtenthaler, R. N.; Gomes de Azevedo, E. *Molecular Thermodynamics of Fluid-Phase Equilibria,* 3rd ed: Prentice Hall Inc.: Engelwood Cliffs, NJ; 1999.

[10] Susana S. Pinto and Hermı´nio P. Diogo, "Energetics of Hydroxybenzoic Acids and of the Corresponding Carboxyphenoxyl Radicals", *J. Phys. Chem. A*, 109, pp.9700-9708, 2005.

[11] Guigard S.E. and Stiver W.H.. A Density-Dependant Solute Solubility Parameter for Correlating Solubilities in Supercritical Fluids. *Ind. Eng. Chem. Res*, 37, pp. 3786–3792,1998.

[12] Vázquez da Silva, M, and Barbosa, D. "Prediction of the solubility of aromatic components of wine in carbon dioxide", *J. Supercritcal.Fluids*, 2004; 31:9-25.

[13] Jie Ke, Can Mao, Minghong Zhong, Buxing Han,and Haike Yan, "solubilities of salicylic acid in SC Co2 with ethanol cosolvent", *J.of Supercritical.Fluids*,9, No 2, 1996.

[14] Frank P. Lucien and Neil R. Foster, "Influence of Matrix Composition on the Solubility of Hydroxybenzoic acid isomers in Supercritical Carbon Dioxide", *Ind. Eng. Chem. Res*, 35, pp. 4686-4699, 1996.

[15] Bamberger, T.; Erickson, J. C.; Cooney, C. L.; Kumar, S. K, "Measurement and Model Prediction of Solubilities of pure fatty acids, pure triglycerides, and mixtures of triglycerides in supercritical carbon dioxide. *J. Chem. Eng. Data*, *33*, 327*,* 1988.

[16] Chang, H.; Morrell, D. G. "Solubilities of Methoxy-1-Tetralone and Methyl Nitrobenzoate Isomers and their mixtures in Supercritical carbon dioxide", *J. Chem. Eng. Data*, *30*, pp. 74-78, 1985.

[17] S T. Chung and K.S. Shing, "Multiphase behavior of binary and ternary systems of heavy aromatic hydrocarbons with supercritical carbon dioxide", *Fluid Phase Equilibria*, 81, pp. 321-341, 1992.

Sciences & Technology **Vol 3** – **N°2**, December 2018, pp. 13-25

EARTH'S TOMOGRAPHY WITH SUPERNOVA NEUTRINOS OSCILLATION IN THE LMA RANGE.

Submited on 16/11/2015 – Accepted on 03/06/2016

Abstract

Low energy neutrinos can be used to probe the Earth's density from the study of the Earth's matter effects on their oscillation. In this work, we will show how this can be achieved with neutrinos coming from a future Galactic Supernova explosion ($D \sim 10\ Kpc$), using an analytic formula that describes the Earth's matter effects on their oscillation. We will focus, in this study, on the linear case where neutrinos travel short distances ($L \ll 1700\ km$) through the Earth, showing how a Tomogram of the Earth (a 2D image from a 3D body) can be created just by making use of the information obtained from the observation of the Earth's matter effects, which is the case for specific choices of the neutrino oscillation parameters and the neutrino mass schemes. In our work, we will treat the case where the neutrino oscillations are explained by the large mixing angle solution to the solar neutrino problem (LMA), combined with the normal mass hierarchy.

Keywords: *Supernova neutrinos, neutrino oscillation, Earth's matter effects.*

S LEBBAL [1]
J MIMOUNI [2]

1 Laboratory of Physics of Radiation and their Interactions with Matter (PRIMALAB), University Batna 1, Algeria.

2 Laboratory of Mathematical Physics and Subatomic Physics (LPMPS), Frères Mentouri University, Algeria.

INTRODUCTION :

Neutrino Tomography opens new possibilities to probe the Earth's interior, since neutrino physics is sensitive to the density of the matter travelled, unlike seismic geophysics which is sensitive to the density jumps. Depending on the propagation model, from the source to the detector, the neutrino tomography can be divided into two techniques [1], whether based on the interaction of neutrinos with the Earth's matter which manifests as the attenuation of the flux for high energy neutrinos (above TeV) [2], or on the Earth's matter effects on their oscillations for low energy ones (MeV to GeV). The first technique is known as NAT (Neutrino Absorption Tomography), and the second is known as NOT (Neutrino Oscillation Tomography).

Depending on the medium where they are first produced, NOT technique can be applied differently:

1. neutrinos produced in vacuum (Atmospheric neutrinos), or from man-made sources, do not have to go through dense matter, so, they reach the surface of the Earth as they are produced. The only matter that affects their oscillations is the Earth's ([1], [3], [4]). This method allows the construction of symmetric density profiles only.

2. neutrinos emerged from a stellar medium (The Sun or a Supernova), undergo the so-called MSW effect: they are produced at the core as flavor eigenstates, and have to pass –on their way out- by different layers (resonant layers) of different densities before travelling through the vacuum, to reach eventually the Earth as mass eigenstates.

In this work, we will focus on the second technique, which depends strongly on the Earth Matter Effects (EME) on the oscillation of Supernova (solar) neutrinos, trying to reproduce the Earth's density profile assuming that nothing is known about it, and that the only information we have is the neutrinos'.

An analytic formula that describes the EME on the oscillation of supernova neutrinos is obtained for the linear regime (, where a simple dependence of these effects on the matter induced potential allows one to notice that the EME analytic formula is a Fourier transform of , and then, by performing a Fourier transformation, we obtain the information sought for (. In doing so, some obstacles are met, most importantly, the lack of knowledge of the neutrino energies (especially from above). We will detail how it is dealt with, by invoking an iteration procedure that allows one to reach the "exact" profile after obtaining a series of potentials (four potentials for the solar case [5]).

In this paper, we will focus on Supernova neutrinos, which have higher energies from above (on the high energy tail of the spectrum). We will start (sec.II) with the neutrino evolution inside the SN, describing how the SN matter affects their oscillation (the MSW effect) before they leave it to travel through vacuum on their way to the Earth. After the neutrinos reach the Earth, their oscillation gets affected by the Earth's matter. We derive, in (sec.III) a theoretical formula that describes these effects, and we apply it to short distances travelled through the Earth (the linear regime). The results are presented in (sec IV) for three Earth density profiles: the Step-like, PREM (Preliminary Reference Earth Model) and an asymmetric step-like density profiles, showing by that how by making use of the Supernova neutrinos data, a tomogram of the Earth can be created.

II. Neutrino evolution inside the Supernova:

Neutrinos are produced in the core of the Supernova, and travel through its mantle and envelope on their way out. Being low energy neutrinos, they are transparent to the matter they go through (from the interaction perspective),

thus one cannot expect much carried information, although, the oscillation phenomenon can bring information because the resonant oscillation depends on the density profile around the resonant point, which is the key ingredient to our study.

From the onset of the gravitational collapse to the explosion, neutrinos undergo several property changes, all happening before leaving the SN envelope. The original properties are expected from SN simulations, and any change whatsoever in them, testifies for neutrino conversion inside the SN and the SN matter effects on them.

Neutrino fluxes evolve with time. This main feature helps us to recognize the existence of three major phases in the evolution of the rates. Each phase is related to a well known process of emission [6].

The flavor eigenstate neutrino produced in the SN, emerges from it as mass eigenstate, after passing through a resonant region which is responsible for this kind of conversion.

In the case of solar neutrinos, only one resonant neutrino oscillation occurs in the star [7], however in the Supernova case, neutrinos go through two resonant points, because the core density is sufficiently high. The resonance density is proportional to the mass difference:

$$\rho_{res} \sim 1.4\times10^{6} g/cc \left(\frac{\Delta m^2}{1eV}\right)\left(\frac{10\ MeV}{E}\right)\left(\frac{0.5}{Y_e}\right)\cos 2\theta \quad \text{(II. 1)}$$

- The layer at higher densities (H-resonance layer) which corresponds to Δm^2_{atm} is at

$$\rho_H \sim 10^3 - 10^4 g/cc \qquad \text{(II. 2)}$$

- The layer at lower densities (L-resonance layer), characterized by Δm^2_{sol} is at :

$$\rho_L = \begin{cases} 5-15\ g/cc \\ 10-30\ g/cc \\ < 10^{-4} g/cc \end{cases} \qquad \text{(II.3)}$$

Which correspond respectively to the LMA, SMA, and VO solutions to the solar neutrino problem.

The transition regions are far outside the core of the SN, and occur mainly in the outer layers of the mantle. The dynamics of conversions in the two resonance layers can be considered independently, and each transition is reduced to a two neutrino problem:

- In the H-resonance layer, the mixing U^m_{e2} associted with Δm^2_{sol} is suppressed by the matter. The suppression factor is:

$$\frac{U^m_{2e}}{U_{2e}} \sim \frac{\rho_L}{\rho_H} \lesssim 10^{-2} \qquad \text{(II.4)}$$

Correspondingly, the effects driven by Δm^2_{sol} are suppressed by a factor of two.

- In the L-resonance layer, the mixing associated with U^m_{3e} coincides with vacuum mixing ($U^m_{3e} \approx U_{3e}$).

Therefore, the level ν_3 does not participate in the dynamics: it decouples from the rest of the system, and the problem is reduced to a two state problem.

The dynamics of transitions in each layer is determined by the adiabaticity parameter γ:

$$\gamma = \frac{1}{2n}\left(\frac{\Delta m^2}{E}\right)^{1-\frac{1}{n}} \frac{\sin^2 2\theta}{(\cos 2\theta)^{1+\frac{1}{n}}}\left(\frac{2\sqrt{2}G_F Y_e}{m_N}A\right)^{1/n} \qquad \text{(II.5)}$$

Such that the probability that a neutrino jumps from one matter eigenstate to another (the flip probability) is given by [8]:

$$P_f = exp\left[-\left(\frac{E_{na}}{E}\right)^{2/3}\right] \qquad \text{(II.6)}$$

Where

$$E_{na} = \left(\frac{\pi}{12}\right)^{3/2} \frac{\Delta m^2 \sin^2 2\theta}{\cos^2 2\theta}\left(\frac{2\sqrt{2}G_F Y_e}{m_N}A\right)^{1/2} \qquad \text{(II.7)}$$

(Figure. 1) illustrates how we can divide the whole range of energy into three parts:

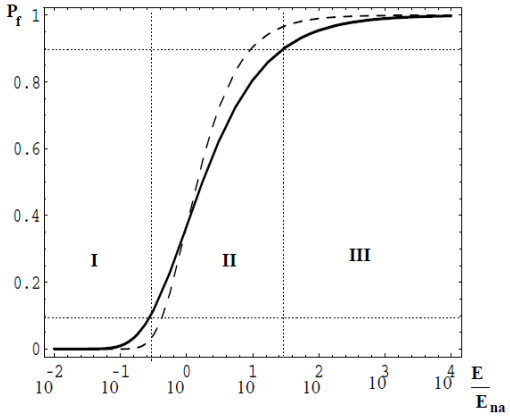

Fig. 1. The dependence of P_f on E/E_{na}(the solid line is for the density profile $\rho \sim r^{-3}$, and the dashed line is for a density profile $\rho \sim e^{-r}$) [8]

1. **Region I:** $(E/E_{na} < 10^{-1})$

Where pure adiabatic conversion occurs: $P_f \approx 0$.

2. **Region III:** $(E/E_{na} > 10^{2})$

This region corresponds to a strong violation of adiabaticity: $P_f \approx 1$

3. **Region II:** $(E/E_{na} = 10^{-1} - 10^{2})$

In this region (the transition region), the adiabaticity breaking increases with E (P_f increses with the increase of the neutrino energy). For our case of density distribution profile ($\rho \sim r^{-3}$), the transition region does not depend strongly on the neutrino energy, compared to the case of the Sun ($\rho \sim e^{-r}$), where the transition region spans only about two orders of magnitude (P_f depends strongly on the neutrino energy).

The observable part of the SN neutrino spectrum spans about one order of magnitude. If the spectrum is in region I, completely adiabatic conversion occurs for the whole spectrum. In the region II, the conversion depends on the energy, however, the dependence is not strong over the relevant range of energies.

(Figure. 2) shows the contours of equal P_f in the $(\Delta m^2, sin^2 2\theta)$-plot for energies E=5 MeV and E=50 MeV. The neutrinos belonging to the same line (determined by the couple $(\Delta m^2, sin^2 2\theta)$) have the same P_f.

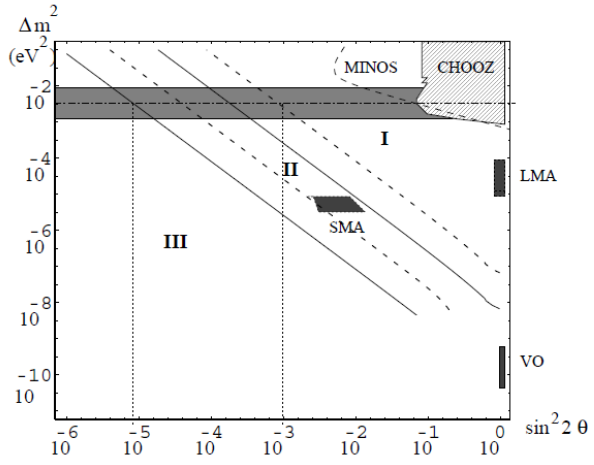

Fig. 2: Contours of equal P_f in the $(\Delta m^2, sin^2 2\theta)$-plot for two different energies on the borders of the observable spectrum (Solid lines for 5 Mev, and dashed lines for 50 Mev). [8]

The contours of $P_f \approx 0.1$ (adiabatic transitions) and $P_f \approx 0.9$ (highly non-adiabatic transitions) divide the plot into three regions:

- The adiabatic region: is the region above the contour $P_f \approx 0.1$, where the adiabaticity is satisfied and strong flavor conversions occur. The LMA solution lies in this region.
- The transition region: is the region between $P_f \approx 0.1$ and $P_f \approx 0.9$ contours. In this region, the adiabaticity is partially broken, and the transitions are not complete. Moreover, the extent of transitions depends on the energy.
- The non-adiabatic region: is the region below the contour $P_f \approx 0.9$. The neutrino conversions are practically absent.

Each neutrino mass and flavor spectrum can be presented by two points in the $(\Delta m^2, sin^2 2\theta)$-plot, which characterizes the layers H and L. One corresponding to $(\Delta m^2_{31}, sin^2 2\theta_{e3})$, should lie in the atmospheric band, and the other one should lie in one of the "islands" corresponding to the solutions of the solar neutrino problem.

The H-resonance is in the adiabatic range for $sin^2 2\theta_{e3} \approx 4|U_{e3}|^2 \gtrsim 10^{-3}$,

and in the transition region for

$10^{-5} \lesssim sin^2 2\theta_{e3} \lesssim 10^{-3}$.

Now, to follow the neutrino conversion inside the SN, we need to reconstruct the neutrino mass spectrum (which is described by a two points in the $(\Delta m^2, sin^2 2\theta)$-plane), but, due to the multiplicity of the possible schemes (six possible schemes of neutrino masses and mixings), which are related to the multiple solutions there are to the solar neutrino problem, the unidentified type of mass hierarchy and the unknown yet precise value of U_{e3}, we will limit this study to one possible scheme (of our choice) from which we extract the neutrino (antineutrino) survival probabilities.

We focus on the scheme of the LMA solution and the normal mass hierarchy, within which, the predictions depend on the value of U_{e3}.

The antineutrinos are represented on the same level crossing diagram, as neutrinos travelling through matter with "effectively" negative n_e, because their effective potential V has an opposite sign.

For the normal mass hierarchy, and as long as the solar neutrino solution is LMA, both resonances (L and H) lie in the neutrino channel (Figure. 3):

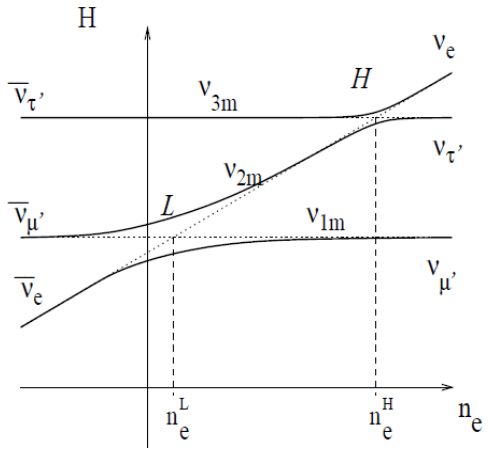

Fig. 3. Level crossing scheme for the LMA solution and the normal mass hierarchy [8].

Taking into account that the dynamics of transitions in the two resonance layers are independent, the fluxes of neutrino mass eigenstates at the surface of the star can be written down directly by tracing the path of the neutrino in the level crossing diagram. The fluxes are expressed in terms of P_L, P_H, $\bar{P}_L$, $\bar{P}_H$ (flip probabilities for neutrinos (antineutrinos) in L, H-resonance layers)

$$\begin{pmatrix} F_e \\ F_{\bar{e}} \\ 4F_x \end{pmatrix} = \begin{pmatrix} p & 0 & 1-p \\ 0 & \bar{p} & 1-\bar{p} \\ 1-p & 1-\bar{p} & 2+p+\bar{p} \end{pmatrix} \begin{pmatrix} F_e^0 \\ F_{\bar{e}}^0 \\ F_x^0 \end{pmatrix} \tag{II.8}$$

F_i^0 are the initial neutrino fluxes for the i-flavor as produced in the core of the star.

F_i are the neutrino fluxes at the surface of the star.

$p, \bar{p}$ are the survival probabilities of electron neutrinos (antineutrinos).

The neutrino fluxes arise from the central parts of the SN (high density regions) where all the mixings are highly suppressed. The initial neutrino flavor states coincide then with the matter eigenstates.

Using the level crossing scheme (fig. 3), we derive the following general expressions for the electron neutrinos survival probabilities [8]:

- For neutrinos:

$$p = |U_{e1}|^2 P_H P_L + |U_{e2}|^2 (P_H - P_H P_L) + |U_{e3}|^2 (1 - P_H) \tag{II.9}$$

- For antineutrinos

$$\bar{p} = |U_{e1}|^2 (1 - \bar{P}_L) + |U_{e2}|^2 \bar{P}_L \tag{II.10}$$

For the LMA solution, the solar neutrino data is explained via the $\nu_e \to \nu_2$ resonant conversion inside the sun with a large mixing angle:

$$sin^2 2\theta_{sol} = 0.7 - 0.95 \approx 1 \tag{II.11}$$

For the case of the LMA solution ($P_f \equiv P_L = \bar{P}_L \approx 0.1$) and the normal mass hierarchy (Fig.3), antineutrinos do not encounter any resonance ($\bar{P}_H = 0$), even though, there is a significant $\nu_e \leftrightarrow \nu_2$ conversion due to the large mixing angle! The evolution thus is adiabatic in both L and H layers in this channel.

The following transitions occur:

$$\bar{\nu}_e \to \bar{\nu}_1, \qquad \bar{\nu}_{\acute{\mu}} \to \bar{\nu}_2, \qquad \bar{\nu}_{\acute{\tau}} \to \bar{\nu}_3$$

The survival probability for $\bar{\nu}_e$ is then:

$$\bar{p} \approx |U_{e2}|^2 \approx cos^2 \theta_{sol} \tag{II.12}$$

In the neutrino channel, $P_L \approx 0$ (LMA lies in region I)

$$p \approx |U_{e2}|^2 P_H + |U_{e3}|^2 (1 - P_H) \tag{II. 13}$$

The expression of the survival probability of ν_e contains thus the flip probability in the H-resonance layer. So, depending on the value of P_H, the neutrino survival probability takes values between

$$|U_{e3}|^2 \leq p \leq |U_{e2}|^2$$

Region I: ($P_H = 0$)

The level crossing scheme leads to the following transitions:

$$\nu_e \to \nu_3, \qquad \nu_{\acute{\mu}} \to \nu_1, \quad \nu_{\acute{\tau}} \to \nu_2$$

From (II.9), the electron neutrino survival probability is then:

$$p \approx |U_{e3}|^2 \leq 0.03 \tag{II.14}$$

The flavor transitions in this region are thus complete.

Region II:

In this region, the following transitions occur

$$\nu_e \to \nu_2, \nu_3 \qquad \nu_{\acute{\mu}} \to \nu_1 \qquad \nu_{\acute{\tau}} \to \nu_2, \nu_3$$

The neutrino survival probability is given by:

$$p \approx |U_{e2}|^2 P_H \tag{II.15}$$

Region III:

The H-resonance is inoperative ($P_H = 1$):

$$p \approx |U_{e2}|^2 \approx 0.2 - 0.4 \qquad \text{(II.16)}$$

The following transitions occur:

$$\nu_e \to \nu_2 \qquad \nu_{\bar{\mu}} \to \nu_1 \qquad \nu_{\bar{\tau}} \to \nu_3$$

Thus, for the normal mass hierarchy and the LMA solution, the survival probabilities for both neutrinos and antineutrinos are summarized in (Table. 1)

Regions where the value of P_H lies	p	$\bar{p}$
Region I	$\|U_{e3}\|^2$	$cos^2\theta_{sol}$
Region II	$P_H\, sin^2\theta_{sol}$	$cos^2\theta_{sol}$
Region III	$sin^2\theta_{sol}$	$cos^2\theta_{sol}$

Tab.1: Survival probabilities for the LMA solution ($P_L = \bar{P}_L = 0$)

In vacuum, and on the way to the Earth, any coherence between the mass eigenstates is lost due to the divergence of the wavepackets. Indeed, over a distance D, the two wavepackets corresponding to two mass eigenstates with a given Δm^2 and having an energy E separate from each other by a distance $\Delta d = \frac{\Delta m^2}{2E^2} D$. The lengths of the individual wavepackets are:

$\sigma \lesssim \frac{1}{T} \approx 10^{-11} cm$, Where T is the temperature of the production region.

So, even for the smallest $\Delta m^2 \sim 10^{-10} eV^2$, for $E = 10MeV$, and $D = 10Kpc$, the two wavepackets sepearte from each other by a distance $\Delta d = 10^{-2} cm$, which is way larger than the lengths of the individual wavepackets ($\Delta d \gg \sigma$). This leads to conclude that neutrinos are not affected by the vacuum they propagate through, and that they reach the surface of the Earth as incoherent fluxes of the mass eigenstate (mixed flavors).

III. Neutrino evolution inside the Earth :

The Earth Matter Effects on the oscillation of neutrinos have been extensively studied [9], whether making use of one detector [10], two or even more detectors [11].

The neutrino trajectory inside the Earth, before reaching the detector, depends on the location of the SN with respect to the detector on Earth.

We will imagine a scenario where the SN faces a detector, which measures the neutrino flux as they reach the surface of the Earth (the same that emerges from the SN envelope) before crossing the Earth (no Earth matter effects), and another one shielded by the Earth, which measures the flux with the Earth's matter effects (figure. 4).

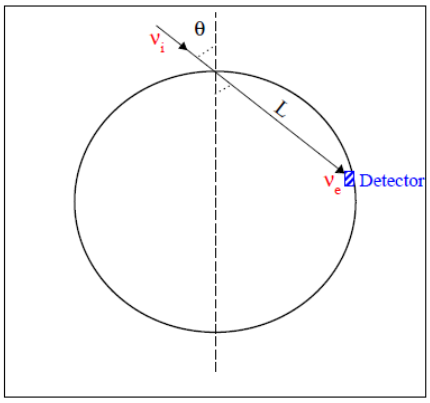

Fig. 4. Mass to flavor transition inside the Earth.

To every mass eigenstate flux reaching the Earth's surface, there are three contributions to this flux coming from the three falvor eigenstates produced in the SN.

The flux of ν_e at the detector (after traversing the Earth) is:

$$F_e^D = \sum_i P_{ie} F_i \qquad \text{(III.1)}$$

Where:

P_{ie} is the probability that a mass eigenstate ν_i entering the Earth reaches the detector as ν_e.

F_i: is the flux of mass eigenstates emerging from the SN envelope, and the same reaching the Earth's surface.

Equation (III.1) can be written also:

$$F_e^D = P^D F_e^0 + (1 - P^D) F_x^0 \qquad \text{(III.2)}$$

P^D is the neutrino survival probability at the detector.

$$P^D \equiv \sum_i a_i P_{ie} \qquad \text{(III.3)}$$

$$P \equiv \sum_i |U_{ei}|^2 a_i \qquad \text{(III.4)}$$

$$\begin{cases} a_1 = P_H P_L \\ a_2 = P_H(1-P_L) \\ a_3 = 1-P_H \end{cases} \quad \text{(III.5)}$$

From (III.2) the difference in the ν_e fluxes at the detector due to the propagation in Earth is:

$$F_e^D - F_e = (P^D - P)(F_e^0 - F_x^0) \quad \text{(III.6)}$$

Where:

F_e^0 is the original neutrino flux (as produced inside the SN).

F_e the flux that reaches the Earth's surface.

F_e^D the electron neutrino flux after traversing the Earth.

$F_x^0 \equiv F_\mu^0 \equiv F_\tau^0$ are the original fluxes of the non electronic neutrinos in the SN.

P is the neutrino survival probability at the surface of the Earth (envelope of the Supernova).

From (III.3), (III.4) and (III.5):

$$P^D - P = P_H(P_{2e} - |U_{e2}|^2)(1-2P_L) + (P_{3e} - |U_{e3}|^2)(1-P_H - P_H P_L) \quad \text{(III.7)}$$

Inside the Earth ν_3 oscillates with a very small depth:

$$P_{3e} - |U_{e3}|^2 \lesssim \left(\frac{2EV_{Earth}}{\Delta m^2_{atm}}\right) sin^2 2\theta_{e3} \quad \text{(III.8)}$$

V_{Earth} is the effective potential of ν_e in the Earth.

For SN neutrinos, $\frac{2EV_{Earth}}{\Delta m^2_{atm}} \lesssim 10^{-2}$.

Moreover, $sin^2 2\theta_{e3} \leq 0.1$. So that

$$P_{3e} - |U_{e3}|^2 \leq 10^{-3} \quad \text{(III.9)}$$

So the second term in the equation (III.7) can be neglected, and the fluxes difference can be written for the normal mass hierarchy and the LMA solution case ($P_L = \bar{P}_L \approx 0$):

- for neutrinos

$$F_e^D - F_e = P_H(P_{2e} - |U_{e2}|^2)(F_e^0 - F_x^0) \quad \text{(III. 10)}$$

- for antineutrinos

$$F_{\bar{e}}^D - F_{\bar{e}} = (\bar{P}_{1e} - |U_{e1}|^2)(F_{\bar{e}}^0 - F_x^0) \quad \text{(III. 11)}$$

P_{2e} is the probability that the mass eigenstate ν_2 entering the Earth, reaches the detector as ν_e.

Note that for the inverted mass hierarchy, the expressions of the flux differences have the same form, with substitution: $\nu \leftrightarrow \bar{\nu}$, $P_H \leftrightarrow \bar{P}_H$ and $P_L \leftrightarrow \bar{P}_L$.

Clearly the Earth matter effects are observed in the regions II and III (figure. 1) for the neutrino channel, where the transition in the H-resonance is purely non-adiabatic ($P_H \neq 0$), and for antineutrinos where the H-resonance is inoperative (for our chosen case).

The Earth matter effects are encoded in the quantity $(\bar{P}_{1e} - |U_{e1}|^2)$ for antineutrinos, and in $(P_{2e} - |U_{e2}|^2)$ for neutrinos. So we turn now to the calculation of this quantity.

- P_{2e} ($\bar{P}_{1e}$) is the probability that a mass eigenstate neutrino is found at the detector as an electron flavor neutrino after traversing a distance L inside the Earth.
- $|U_{e2}|^2$ ($|U_{e1}|^2$) is the projection of the mass eigenstate onto the electron flavor state.

To calculate the regeneration factor, we need to write the neutrino evolution equation in the flavor basis [12]

$$i\frac{d}{dt}\nu = [U\, diag(0, 2\delta, 2\Delta)\, U^+ + diag(V(t), 0, 0)]\nu \quad \text{(III. 13)}$$

Where:

$\nu = (\nu_e, \nu_\mu, \nu_\tau)^T$ is the wave function of the neutrino system.

t: is the coordinate along the neutrino trajectory.

$V(t) = \sqrt{2}G_F N_e(t)$: is the neutrino matter induced potential.

For our purpose, it is convenient to go to the new basis defined through:

$\nu \equiv O_{23}\Gamma_\delta O_{13}\tilde{\nu}$. Then the neutrino evolution equation for the rotated state $\tilde{\nu}$ is:

$$i\frac{d}{dt}\begin{pmatrix}\tilde{\nu}_1\\ \tilde{\nu}_2\\ \tilde{\nu}_3\end{pmatrix}=\begin{pmatrix}2S_{12}^2\delta+C_{13}^2V(t) & 2S_{12}C_{12}\delta & S_{13}C_{13}V(t)\\ 2S_{12}C_{12}\delta & 2C_{12}^2\delta & 0\\ S_{13}C_{13}V(t) & 0 & 2\Delta+V(t)S_{13}^2\end{pmatrix}\begin{pmatrix}\tilde{\nu}_1\\ \tilde{\nu}_2\\ \tilde{\nu}_3\end{pmatrix}$$

Where:

$C_{ij}\equiv\cos\theta_{ij}$ and $S_{ij}\equiv\sin\theta_{ij}$

$\Delta=\frac{\Delta m_{32}^2}{4E}$

$\delta=\frac{\Delta m_{21}^2}{4E}$ (III. 14)

Neutrino evolution inside both the Supernova (Sun) and the Earth is adiabatic

($V\lesssim 2\delta\ll 2\Delta$) (III. 15)

In addition, since $S_{13}\ll 1$, we can to a very good accuracy neglect the (1-3) and (3-1) elements of the effective Hamiltonian compared to the (3-3) element:

$$i\frac{d}{dt}\begin{pmatrix}\tilde{\nu}_1\\ \tilde{\nu}_2\\ \tilde{\nu}_3\end{pmatrix}\approx\begin{pmatrix}2S_{12}^2\delta+C_{13}^2V(t) & 2S_{12}C_{12}\delta & 0\\ 2S_{12}C_{12}\delta & 2C_{12}^2\delta & 0\\ 0 & 0 & 2\Delta\end{pmatrix}\begin{pmatrix}\tilde{\nu}_1\\ \tilde{\nu}_2\\ \tilde{\nu}_3\end{pmatrix}$$

(III. 16)

This means that the third matter eigenstate decouples from the other two matter eigenstates. Besides, the (3-3) element in the Hamiltonian (III.16) shows that the Earth matter effects on the third mass eigenstate are negligible.

Let us now introduce the neutrino evolution matrix in the rotated basis according to:

$$\tilde{\nu}(t)=\tilde{S}(t,t_0)\tilde{\nu}(t_0)\qquad\text{(III.17)}$$

$$\tilde{S}(t_0,t_0)=\begin{pmatrix}1 & & \\ & 1 & \\ & & 1\end{pmatrix}$$

The matrix $\tilde{S}(t,t_0)$ satisfies the same evolution equation as the rotated state $\tilde{\nu}$:

$$i\frac{d}{dt}\left(\tilde{S}(t,t_0)\tilde{\nu}(t_0)\right)=H\tilde{S}(t,t_0)\tilde{\nu}(t_0)$$

The decoupling of the third matter eigenstate implies that the evolution matrix is written as:

$$\tilde{S}(t,t_0)=\begin{pmatrix}\tilde{\alpha}(t,t_0) & \tilde{\beta}(t,t_0) & 0\\ -\tilde{\beta}^*(t,t_0) & \tilde{\alpha}^*(t,t_0) & 0\\ 0 & 0 & f(t,t_0)\end{pmatrix}$$

(III.18)

Where

$$f(t,t_0)=exp[-2i\Delta(t-t_0)]\qquad\text{(III.19)}$$

Probabilities P_{1e} and P_{2e} in terms of $\tilde{\alpha}$, $\tilde{\beta}$:

$$\bar{P}_{1e}=C_{13}^2\left|C_{12}\tilde{\alpha}-S_{12}\tilde{\beta}\right|^2$$

$$P_{2e}=C_{13}^2\left|S_{12}\tilde{\alpha}+C_{12}\tilde{\beta}\right|^2$$

Finally, the Earth regeneration factor is expressed by:

$$P_{2e}-|U_{e2}|^2=C_{13}^2\left[\cos 2\theta_{12}\left|\tilde{\beta}\right|^2+\sin 2\theta_{12}Re\left(\tilde{\alpha}^*\tilde{\beta}\right)\right]$$

(III.20)

The expression (III.20), is valid for an arbitrary density profile, and reproduces all the analytic expressions obtained under simplified assumptions about the Earth's density profile (matter of constant density, three layers of constant densities and the adiabatic approximation) [12].

Note:

The quantities P_{ei}, $|U_{ei}|^2$ and P_{ie} satisfy the condition:

$$\sum_{i=1}^3 P_{ei}=\sum_{i=1}^3|U_{ei}|^2=\sum_{i=1}^3 P_{ie}=1$$

(III.21)

Since $P_{3e}=|U_{e3}|^2$ (Earth matter effects on the third mass eigenstate are negligible), (III. 21) gives:

$$P_{1e}-|U_{e1}|^2=-(P_{2e}-|U_{e2}|^2)\qquad\text{(III.22)}$$

Now, to obtain the explicit expression for the regeneration factor, we have to find the explicit expressions for both $\tilde{\alpha}$, $\tilde{\beta}$ witch are valid for an arbitrary Earth density profile. The basic point is that the neutrino potential inside the Earth is small, and so can be considered as perturbation.

For that, we need to perform the perturbation theory in V [13] for the evolution matrix (III. 18), which requires -for its validity- the smallness of two dimensionless parameters:

- $\frac{V}{2\delta}$ which is indeed very small in our case (III. 15)

- $VL = \int_0^L V dx$ which can be large enough for long distances travelled by neutrinos through the Earth.

The effective Hamiltonian (III.16), can be decomposed as $\tilde{H}(t) = \tilde{H}_0 + \tilde{H}_1(t)$, Where $\tilde{H}_0$ and $\tilde{H}_1(t)$ are of zeroth and first order in V(t) respectively.

To first order in V(t), the evolution matrix $\tilde{S}(t, t_0)$ can be written as:

$$\tilde{S}(t,t_0) \approx \tilde{S}_0(t,t_0) - i\tilde{S}_0(t,t_0)\int_{t_0}^{t}\left[\tilde{S}_0(t,t_0)^{-1}\tilde{H}_1(t)\tilde{S}_0(t,t_0)\right]dt \quad \text{(III.23)}$$

For the zeroth-order matrix $\tilde{S}_0(t,t_0)$ we find ($\tilde{\alpha}_0$, $\tilde{\beta}_0$), we substitute them in (III.23) to find ($\tilde{\alpha}$, $\tilde{\beta}$), which we substitute in (III.20) to get the explicit expression of the regeneration factor [12]:

$$P_{2e} - |U_{e2}|^2 = \frac{c_{13}^4}{2} sin^2 2\theta_{12} \int_0^L dx\ V(x) \sin[2\delta(L-x)] \quad \text{(III. 24).}$$

x is the coordinate of the neutrino path length inside the Earth, and $L = 2R\cos\theta_Z$, where R is the Earth's radius and θ_Z is the zenith angle of the neutrino trajectory (Figure. 4).

We should remind here that the expression (III. 24) is valid for only short distances travelled by neutrinos through the Earth.

A more accurate formula can be obtained by replacing the integrant in (III.24), the in-vacuum oscillation phase, by the corresponding adiabatic one, i.e.

$$P_{2e} - |U_{e2}|^2 = \frac{c_{13}^4}{2} sin^2 2\theta_{12} \int_0^L dx\ V(x) \sin\left[2\int_x^L w(\acute{x})d\acute{x}\right] \quad \text{(III. 25)}$$

This result is obtained by performing the perturbation theory in $\frac{V}{2\delta}$ rather than in V. This theory requires only the smallness of $\frac{V}{2\delta}$, regardless of the neutrino path lengths inside the Earth (see [12] appendix A).

Equation (III. 24) can be written:

$$P_{2e} - |U_{e2}|^2 = \frac{c_{13}^4}{2} sin^2 2\theta_{12} f(\delta) \quad \text{(III. 26)}$$

Where

$$f(\delta) = \int_0^L dx\ V(x) \sin[2\delta(L-x)] \quad \text{(III. 27)}$$

$f(\delta)$ has a Fourier integral form and actually means that in the limit of small V, this function is just the Fourier transform of the matter induced potential:

$$V(x) = \frac{4}{\pi}\int_0^\infty d\delta\ f(\delta) \sin[2\delta(L-x)] \quad \text{(III. 28)}$$

There are some limitations of this result that should me mentioned:

- The found result is valid only in the limit $\frac{V}{2\delta} \ll 1$ and $VL \ll 1$.
- The function $f(\delta)$ has to be known precisely in the whole interval $0 \le \delta < \infty$ (which means (II.14) the whole energy interval $0 \le E < \infty$). Although, it is only measured in a finite energy interval, and with some experimental errors, because the detectors have finite energy resolution, and can give limited information on the energy of the incoming neutrinos, and the neutrino parameters.
- The precision in the neutrino oscillation parameters $\Delta m_{21}^2, \theta_{12}$ and θ_{13} are only known with certain experimental uncertainties.

IV. Procedure and results

For the matter density in the upper mantle of the Earth, $\rho \approx 3g/cm^3$, the condition $VL \ll 1$ leads to the upper limit on the allowed neutrino path lengths inside the Earth $L \ll 1700\ Km$. This condition will be relaxed in the study of the non linear regime.

Before getting started with the procedure, let us resume and rewrite the needed expressions for neutrinos and antineutrinos. We should remind here that we have limited the study to the LMA solution and the normal mass hierarchy.

- for neutrinos

From (III.26), (III.10) can be written

$$F_e^D - F_e = P_H\left(\frac{c_{13}^4}{2} sin^2 2\theta_{12} f(\delta)\right)(F_e^0 - F_x^0) \quad \text{(IV.1)}$$

- for antineutrinos

From (III.22) and (III.26), (III.11) can be written

$$F_{\bar{e}}^D - F_{\bar{e}} = \left(\frac{c_{13}^4}{2} sin^2 2\theta_{12} f(\delta)\right)(F_{\bar{e}}^0 - F_x^0) \quad \text{(IV.2)}$$

$f(\delta)$ is a quantity that is measured experimentally is only known for a finite interval $\delta_{min} \leq \delta \leq \delta_{max}$ and thus (III.14) a finite interval of neutrino energies: $E_{min} \leq E \leq E_{max}$.

The integral (III.28) requires that f is precisely measured for the whole interval $0 \leq \delta < \infty$ (in the infinite interval of neutrino energies $0 \leq E < \infty$), but since the neutrino energy is limited from above, we will see how this obstacle can be overcome.

First, let us consider an integral of the form (III.28)

$$\frac{4}{\pi}\int_{\delta_{min}}^{\delta_{max}} d\delta\ f(\delta)\sin[2\delta(L-x)]$$

This integral yields

$$\frac{1}{\pi}\int_0^L dy V(y)\left\{\frac{\sin[2\delta(x-y)]}{x-y} - \frac{\sin[2\delta(2L-x-y)]}{(2L-x-y)}\right\}\Bigg|_{\delta_{min}}^{\delta_{max}} \qquad \text{(IV. 3)}$$

In order that this integral approaches the integral over infinite interval $(0 \leq \delta < \infty)$:

$$\begin{cases} V \ll \dfrac{1}{L} \\ V \ll 2\delta \begin{cases} \delta_{max} \to \infty \ \to \delta_{max} \gg \dfrac{1}{L} \gg V \\ \delta_{min} \to 0 \ \to V \ll \delta_{min} \ll \dfrac{1}{L} \end{cases} \end{cases}$$

So, in the ideal case, we would like to have

$$\begin{cases} \delta_{min} L \ll 1 \\ \delta_{max} L \gg 1 \end{cases}$$

As we shall see, having large enough δ_{max} (E_{min}) does not pose any problem. However, in most situations of practical interest, the second condition is not satisfied ($\delta_{min} \gtrsim \frac{1}{L}$). We shall see that this difficulty can be readily overcome.

The fact of having a finite δ_{max} does not affect the procedure. It has been shown [5] that finite δ_{max} leads to a finite coordinate resolution of the reconstructed potential $V(x)$, as well as to small oscillations of the reconstructed potential around the true one. So, for good enough resolution, we can put $\delta_{max} \to \infty$ in our analytic formulas.

There are, though, two reasons why having a sufficiently small δ_{min} may be a fundamental problem:

1. Small δ_{min} implies large neutrino energies, and there are upper limits to the available neutrino energies.

2. The second obstacle is of more fundamental nature. The condition for which our main result is valid, i. e. $\frac{V}{2\delta} \ll 1$, may break down for too small δ_{min} (too high E_{max}). This gives a lower limit to values of δ_{min} one can use ($\delta_{limit} \leq \delta_{min} \to E_{max} \leq E_{limit}$).

To cure the problem posed by having a non zero δ_{min}, we put $\delta_{max} \to \infty$, then from the integral (IV.3) we find:

$$V(x) = \frac{4}{\pi}\int_{\delta_{min}}^{\infty} d\delta\, f(\delta)\sin 2\delta(L-x) + \frac{1}{\pi}\int_0^L dy V(y) F(x,y;2\delta_{min}) \qquad \text{(IV. 4)}$$

Where the function $F(x,y;2\delta_{min})$ is defined as:

$$F(x,y;2\delta_{min}) = \frac{\sin 2\delta_{min}(x-y)}{x-y} - \frac{\sin 2\delta_{min}(2L-x-y)}{2L-x-y} \qquad \text{(IV. 5)}$$

By comparing the integral (IV.4) with the integral (III.28), we can consider the second integral in (IV.4) as a compensating term for an error introduced in (III. 28) by having a non-zero lower limit in the integral over δ. This compensating integral cannot be calculated directly, since it contains the unknown potential $V(x)$. This problem can be cured by invoking a simple iteration procedure.

We first note that in the limit $\delta_{min} \to 0$, the first integral in (IV.4) yields $V(x)$ while the second one disappears. Therefore, for not too large values of δ_{min} (not too small values of E_{max}), the first integral gives a very good approximation to $V(x)$. One can use thus this value to obtain the result to the second part of (IV.4) (the compensating integral) to obtain the next approximation to $V(x)$:

$$V_0(x) = \frac{4}{\pi}\int_{\delta_{min}}^{\infty} d\delta\ f(\delta)\sin[2\delta(L-x)] \qquad \text{(IV.6)}$$

We put:

$$I_0(x) = \frac{1}{\pi}\int_0^L dy V_0(y) F(x,y;2\delta_{min}) \qquad \text{(IV.7)}$$

And then, we calculate the addition:

$$V_1(x) = V_0(x) + I_0(x) \quad \text{(IV.8)}$$

We follow the steps:

$$\begin{cases} I_{n-1}(x) = \frac{1}{\pi}\int_0^L dy V_{n-1}(y)\, F(x,y;2\delta_{min}) \\ V_n(x) = V_0(x) + I_{n-1}(x) \end{cases} \quad \text{(IV. 9)}$$

So, this yields a series of potentials $V_0(x), V_1(x), \dots, V_n(x)$, which for small enough δ_{min} converge to $V(x)$.

For this procedure to work though -in addition to the conditions posed for the linear regime- δ_{min} has to be chosen taking into account the following:

- First, it should be small enough (though possible to reach 0).
- Second, it should be smaller than a critical value δ_c, above which this iteration procedure fails: it yields potentials which, instead of approaching the true profile, they deviate from it ($\delta_{min} \leq \delta_c \rightarrow E_c \leq E_{max}$).

To proceed forward, we should remind that the quantity f (which differs from one profile to another) should be know from the experiment through (IV. 1), but since it is not available yet, here is what we do:

1. We choose a specific density profile of the Earth, from which we generate $f(\delta)$, by making use of the equation (III.27).
2. Then, we pretend that nothing is known about the Earth's density profile, and that the only thing we know is the function $f(\delta)$ (deduced by the step 1), which we use it as our input in the calculation to establish $V(x)$, making use of the formulas {(IV.6)-(IV.9)}.

The calculations are performed following [5], i. e. taking the same conditions used for the solar neutrinos, the only difference we apply here is in the neutrino energies, and more precisely E_{max} (δ_{min}).

The energy of SN neutrinos can be extended up to $70\ MeV$, for which the conditions to be satisfied are:

$$\begin{cases} \delta_{min} = 0.41\ L^{-1} \\ \delta_{max} = 300\ L^{-1} \end{cases} \quad \text{(IV.10)}$$

The critical value for δ_{min} was chosen to be $\delta_c \approx 2.4\ L^{-1}$ ($E_c = 12.5\ MeV$). i.e. the maximum energy has to be at least $12.5\ MeV$ for this iteration procedure to work, which is the case with SN neutrinos.

The precision was taken to be $\varepsilon \approx 3\times10^{-6}$ i.e. $|V(x) - V_n(x)| < \varepsilon$.

The study is performed on three different density profiles (different f) and are presented in what follows:

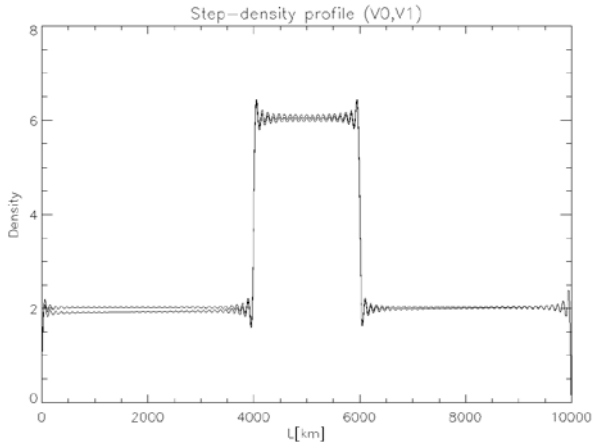

Fig. 5. Step density Profile: $V_0, V_1(\delta_{min} = 0.41L^{-1}, \delta_{max} = 300L^{-1})$

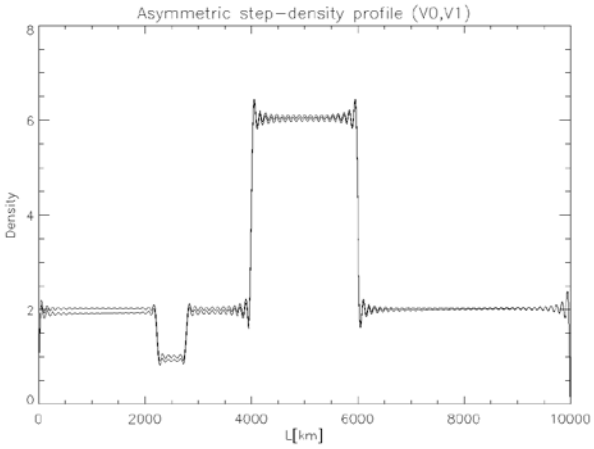

Fig. 6. Asymmetric step density Profile: $V_0, V_1(\delta_{min} = 0.41L^{-1}, \delta_{max} = 300L^{-1})$

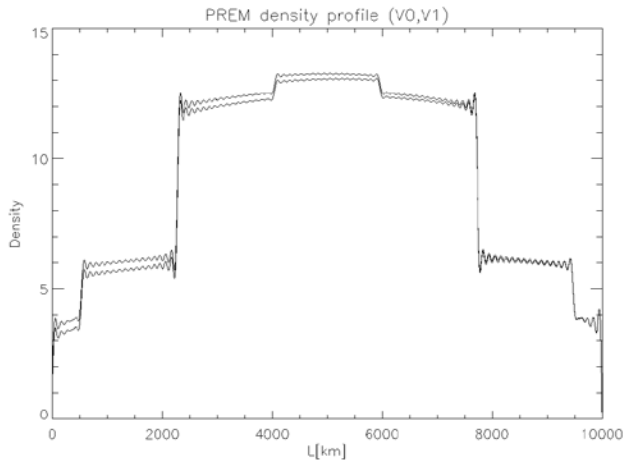

Fig. 7. PREM density Profile [14]: $V_0, V_1 (\delta_{min} = 0.41L^{-1}, \delta_{max} = 300L^{-1})$

V. Analysis:

From the three profiles, the same observation is made:

- All of the Three profiles are produced "exactly" by the first iteration (V_1), regardless their shapes or their density distributions.
- The iterative potentials approach the true profile from below, and never exceed it.
- Even V_0 reproduces the same positions and magnitudes of the density jumps as the true one.
- The deviations of $V_n(x)$ from the exact potential are small at $x \approx L$ and largest at $x = 0$.

This approach not only reproduces the exact positions of the density jumps (already established from seismic geophysics data), but also gives the same magnitudes (the exact value of the densities) in the different layers, so it is complementary to seismic geophysics.

Even if the "true" profile is found from the 1st iteration, V_0 already gives the value of the density near the detector ($x \approx L$).

This procedure allows the reconstruction of even an asymmetric density profile, which can only be achieved for solar and supernova neutrinos due to their particularity of reaching the Earth as mass eignstates.

We should clarify here that by symmetric density profiles we mean profiles that have the same densities around the midpoint of the neutrino trajectory inside the Earth (L). They give rise to potentials that have the same property: $V(L-x) = V(x)$ .This symmetry is only approximate; it is violated by inhomogeneities of the Earth's density distribution on short length scales ([15], [16]).

In the case of solar neutrinos [5], the exact profile was established after the fourth iteration (taking the same conditions here, except for the value of δ_{min} ($E_{max} = 30\ MeV \Longrightarrow \delta_{min} = 3.33\times10^{-3}\ m^{-1}$), so clearly Supernova neutrinos give better (faster) information than Solar neutrinos. In other words, the higher the neutrino energy is, the faster the convergence to the true profile is, and the shorter the time this procedure takes.

VI. The non linear regime:

The previous study was based on the formula (III.24) of the regeneration factor (EME) which was derived after performing the perturbation theory in V. This theory requires the smallness of VL. i.e. short neutrino paths inside the Earth.

The more accurate formula (III.25), however, which was derived by the perturbation theory in $\frac{V}{2\delta}$, does not pose any condition on the length travelled, so, it can be used to probe the Earth's density over "realistic" distances. In other words, one has to employ the inversion procedure based on the expression:

$$f(\delta) = \int_0^L dx\, V(x) \sin\left[2\int_x^L w(\acute{x})d\acute{x}\right] \qquad \text{(VI.1)}$$

Where:

$$w(\acute{x}) = \sqrt{[cos2\theta_{12}\delta - V(x)/2]^2 + \delta^2 sin^2 2\theta_{12}}$$

Since (VI.1) was obtained without making any restriction on the distance travelled, ($\delta_{min}L \ll 1$ does not have to be satisfied here), the matter density profile cannot be found by invoking the previous iteration procedure. The problem becomes very difficult to solve.

The equation (VI.1) is a non-linear Fredholm integral equation of the first kind, and equations of this type are very difficult to solve [17], and need a dedicated study, since they belong to the class of "ill-posed" problems: their solutions are very unstable, and to arrive at a reliable result, one has to invoke special regularization procedures [18]. For non linear integral equations of the first kind, no universal regularization techniques exist.

The NOT technique can also be performed through another approach, which does not rely on the flavor to mass oscillation property that happens to Supernova neutrinos inside the SN, and which distinguishes Supernova (solar) neutrinos from other low energy ones. This approach not only can reveal information about the Earth's matter travelled, but moreover, it allows the probe of the entire Earth ($L = 2R_{Earth} = 12742\ km$) without putting boundaries on the distances neutrinos travel inside. It had been tackled in several papers ([3], [4] and [19]). It makes use of the direct problem rather than trying to solve the

inverse one. It consists of generating random density distribution, dividing it into several layers and then comparing the obtained P_{ab} (theoretically obtained survival probability of the neutrino in the interval [a,b]) with simulated data for the "true" profile (figure. 8). Even though it looks more promising, this approach turned out to be not only a time consuming procedure, but also with limited accuracy!

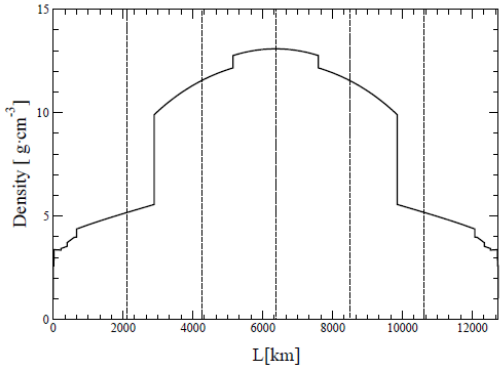

Fig. 8. a. PREM density Profile (step I)

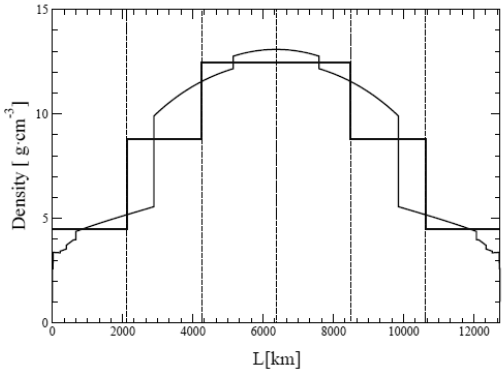

Fig. 8. b. PREM density Profile (step II)

VII. Conclusion :

In an attempt to resolve the inverse problem of neutrino oscillation, we have shown that neutrino oscillation in matter can serve as a powerful tool, not only in revealing information about the matter travelled, but also in probing the 'exact' density values at the different layers travelled. In the case of Supernova neutrinos, and based on their oscillation pattern inside the Supernova, namely the MSW effect, it is achieved through an analytic formula that describes the EME on their oscillation, which, for short distances travelled through the Earth (the linear regime), has a simple (direct) dependence on the neutrino matter induced potential (V). This latter was obtained after invoking an iteration procedure that helped us overcome the problem posed by the limitation (from above) of the neutrino energies. We managed thus, to establish the "true" density profile, for short distances ($L \ll 1700\ km$), in a faster (time conserving) way than the one achieved in the solar neutrino case.

We should mention here that for the chosen neutrino parameters (LMA solution to the solar neutrino problem for the normal mass hierarchy) the study was applicable because the EME on these neutrinos (and antineutrinos) are observed ((III.10),(III.11)), but for other neutrino mass scheme/neutrino oscillation parameters combinations (ex: inverted mass hierarchy/SMA), the situation is quite different: there are cases where these effects are not observed, thus, this study can no longer be applicable. It can, however, still be used the other way around: it can help us reduce the number of the possible neutrino mass schemes, and constrain the neutrino oscillation parameters, depending on the observation of the Earth matter effects.

To go further in this study, we can use the found results (the value of the density) to find the electron density number $N_e(x) = \frac{Y_e}{m_N}\rho(L)$ $(Y_e \approx \frac{1}{2})$ which differs from one element to another, and thus obtain furthermore information about the Earth's composition. We can therefore whether consolidate or refute J. M. Herndon's controversial hypothesis about the existing of radioactive elements, namely Uranium and Thorium at the very center of the Earth's inner core, making thus birth to a sub-inner core that contains these lithophile elements, which –from a geochemical perspective- can never exist in the core of the Earth.

Herndon assumed that these elements are the cause of the Earth's magnetic field, and its instability, and that the energy realized from the decay of these radioactive elements, is the secret behind the heat generated by the Earth ([20], [21], [22]).

Even though this study is performed on distances way smaller than the Earth's distances we want to reach and explore, it allows us to go deeper than the depths reached (so far) by other techniques (digging). It can, thus, be used to reveal information about other "objects" that have "big" diameters and explore their deeper structures, but for the Earth and other objects that have distances comparable to the Earth's, the resolution of the non linear regime will be of a bigger benefit.

References:

[1] W. Winter. Learning about the Earth's interior using the propagation of neutrinos. Earth, Moon and Planets (From the issue entitled "Neutrino Geophysics Proceedings of Neutrino Sciences 2005"). Vol. 99. (2005). pp. 285-307.

[2] M.C. González-García, et al. Radiography of the Earth's core and mantle with atmospheric neutrinos. Phys. Rev. Lett. Vol. 100. (2008).

[3] T. Ohlsson and W. Winter. Reconstruction of the Earth's mantle density profile using a single neutrino baseline. Phys. Lett. B. Vol. 512. (2001). pp. 357.

[4] W. Winter. Probing the absolute density of the Earth's core using a vertical neutrino beam. Phys. Rev. D. Vol. 72. (2005).

[5] E.K. Akhmedov, M.A. Tortola and J.W.F. Valle. Geotomography with solar and supernova neutrinos. JHEP. Vol. 06. (2005). pp. 053.

[6] K. Kotake, et al. Explosion mechanism, neutrino burst and gravitational wavein core collapse Supernovae. Rep. Prog. Phys. Vol. 69. (2006).

[7] A. Yu. Smirnov. The MSW effect and solar neutrinos. preprint, hep-ph/0305106. (2003). < http://arxiv.org/abs/hep-ph/0305106 >

[8] A.S. Dighe and A.Y. Smirnov. Identifying the neutrino mass spectrum from a Supernova neutrino burst. Phys. Rev. D. Vol. 62. (2000).

[9] K. Takahashi, et al. The Earth effects on the Supernova neutrino spectra. Phys. Lett. B. Vol. 510. (2001). pp. 189-196.

[10] A.S. Dighe, et al. Signature of Supernova neutrinos oscillation in the Earth's mantle and core. preprint, hep-ph/0311172 .(2003). < http://arxiv.org/abs/hep-ph/0311172>.

[11] C. Lunardini and A. Yu. Smirnov. Supernova neutrinos: Earth matter effects and neutrino mass spectrum. Nucl. Phys. B. Vol. 616**.** (2001). pp. 307-348.

[12] E.K. Akhmedov, M.A. Tortola and J.W.F. Valle. A simple analytic three-flavor description of the day-night effect in the solar neutrino flux. JHEP. Vol. 05. (2004). pp. 057.

[13] E.K. Akhmedov, et al. Series expansion for three-flavor neutrino oscillation probabilities in matter. JHEP. Vol. 04. (2004). pp. 078.

[14] A.M. Dziewonski and D.L. Anderson. Preliminary reference Earth model. Phys. Earth Planet. Inter. Vol. 25. (1981). pp. 297.

[15] T. Ohlsson and W. Winter. Could one find petroleum using neutrino oscillations in matter?. Europhys. Lett. Vol. 60. (2002). pp. 34-39.

[16] A. N. Ioannisian and A. Y. Smirnov. Matter effects on thin layers: detecting oil by oscillations of solar neutrinos. preprint, hep-ph/0201012. (2002). <http://arxiv.org/abs/hep-ph/0201012 >.

[17] A.H. Borzabadi and O.S. Fard. Approximate solution of nonlinear FIE of the 1st kind. World Academy of Science, Engineering and Technology. Vol. 33. (2007). pp. 70-73.

[18] NAG Fortran Library Chapter Introduction (D05 – Integral Equations) <http://www.nag.co.uk/numeric/FL/manual/xhtml/D05/d05_intro.xml>

[19] M. Lindner, et al. Tomography of the Earth's core using Supernova neutrinos. Astropart. Phys. Vol. 19. (2003). pp. 755.

[20] D.F. Hollenbach and J.M. Herndon. Deep-Earth reactor: nuclear fission, helium and the geomagnetic field. PNAS. Vol. 98. (2001). pp. 11085-11090.

[21] K.R. Rao. Nuclear reactor at the core of the Earth!- A solution to the riddles of relative abundances of helium isotopes and geomagnetic field variability. Current Science. Vol. 82. (2002).

[22] R.J. de Meijer, et al. Quest for a nuclear georeactor. Rad. Phys. Chem. Vol. 71. (2004). pp. 769-774.

NUMERICAL STUDY OF AN INCOMPRESSIBLE LAMINAR FLOW AROUND A NACA AIRFOIL WITH A BLOWING CONTROL.

Submited on 16/01/2018 – Accepted on 03/04/2018

Abstract

A boundary layer separation on a NACA0012 airfoil at a low Reynolds number is numerically investigated. The governing equations are discretized with the finite volume method. The boundary layer separation is examined through the flow structure. Beyond an angle of attack of 8°, a small separation region is detected near the trailing-edge of the airfoil. As the angle of attack increases, the separation region grows up and moves towards the leading edge. In order to control the separation, a parabolic distribution blowing is applied along the separated region. The effectiveness of the control is shown, leading to the improvement of the lift and the lift to drag ratio. As the blowing jet velocity is increased the size of the separation bubble decreases until it disappears.

Keywords: *Boundary layer, Separation control, Aerodynamic performances.*

A BOUNECER
L BAHI

Energy Physics Laboratory, Physics Department, Frères Mentouri University, Algeria.

NOMENCLATURE

C	airfoil chord length
Cd	drag coefficient
Cf	skin friction coefficient
Cl	lift coefficient
Cp	pressure coefficient
h_1	metric parameter in ξ direction
h_2	metric parameter in η direction
P	non-dimensional pressure
Re	Reynolds number
U	horizontal physical velocity
U_0	free-stream velocity
V	vertical physical velocity
Vξ	spanwise computational velocity
Vη	normal computational velocity

Greek symbols

α	angle of attack
ϕ	maximum blowing velocity ratio
τ	non-dimensional time
ρ	density

Subscripts

x	horizontal direction
y	vertical direction
ξ	spanwise direction
η	normal direction to the airfoil

1. INTRODUCTION

The advances in micro-fabrication techniques and miniaturization electronics are leading to the development of small Unmanned Aerial Vehicles (UAVs), Micro-Aerial-Vehicles (MAVs), and small wind turbines. Due to their small length scale of about a few centimeters, the MAV's have the ability to fly in urban settings, tunnels and caves and maintain forward and hovering flight maneuver in constrained environments [1-3]. The small scale of such technological applications combined to their relatively low speed, is the main driving factor for the increasing interest of the low Reynolds number flows over airfoils. Also, this increasing importance is driven by the poor data base of the aerodynamic characteristics of the airfoils operating at low Reynolds numbers (i.e., 10^2-10^5), since most studies on the boundary layer behavior over airfoils have focused on conventional aircraft design with high Reynolds numbers. The boundary layer separation can have a large impact on the performance of any vehicle design.

Laminar separation occurs when a laminar boundary layer is subject to a sufficiently strong adverse pressure gradient. As the pressure increases along the mean flow direction, the flow velocity decreases. If the pressure differential continues, the flow velocity will eventually come to zero and a reversal of the flow will occur [4].

Due to the predominance of viscous effects at low Reynolds number, the flow physics is quite complicated and the boundary layer behaves differently in comparison to its behavior at high Reynolds number. The boundary layer starts to separate at a lower angle of attack as a result of the airfoil curvature changes or the adverse pressure gradient [5]. At a low Reynolds number, the boundary layer often remains laminar in the adverse pressure gradient region and the detached boundary layer may undergo transition to turbulence. The resulting turbulent flow may reattach to the airfoil surface. When the turbulent mixing

momentum is not sufficient, the separated region extends up to the trailing edge [6-7]. The location of the separation point, the size of the separated region and the intensity of the backflow, depend on the flow Reynolds number and the angle of attack of the airfoil. These two parameters determine whether the flow reattaches behind the separated zone or remains separated [8].

At a low Reynolds number, the aerodynamic forces are significantly altered by the boundary layer separation and show a different behavior compared to a high Reynolds number flow [9]. Both drag and lift increase with the angle of attack and at a sufficiently low Reynolds number the stall is absent over a large range of angles of attack [10]. Therefore it is desirable to control the flow through the boundary layer. To delay or eliminate the boundary layer separation in order to reduce the drag and increase the lift, different control concepts can be applied, such as the use of the airfoil shaping to create a favorable pressure field capable to overcome the undesirable adverse pressure gradients. Another control mode can be performed with the addition of an energy momentum to the separated boundary layer, to recover the lost energy. Air suction and blowing, vortex generators, surface cooling and moving walls are some examples of the boundary layer separation control [11]. In the experimental investigations, the control process of the separation over small scale airfoils at low Reynolds number conditions requires a miniature devices and finer measurements, which is complicated and costly, so the numerical simulation is an alternate approach to reduce the time and the cost. Many numerical studies optimizing control parameters, such as the jet location, the size and the jet velocity of the suction/blowing, were conducted researchers [12-15]. Sedar and Kaynak [16] investigated the blowing/suction control effects on NACA2415 airfoil at low Reynolds number conditions for a fixed angle of attack. Results indicated that smaller velocity is better for the blowing case; whereas larger velocity is better for the suction case. The performance of the airfoils can be considerably improved by combining the suction and the blowing control. Brehm et al. [17], show that the simultaneous use of suction and blowing is more effective than using the suction and the blowing separately. Huang et al. [18], studied numerically the suction and the blowing control on NACA0012 airfoil at an angle of attack of 18° and they concluded that suction is different from blowing. While the suction increases the lift by creating a larger and lower pressure zone on the airfoil, leading edge blowing increases lift by generating greater circulation about the separation bubble.

In the present contribution, a CFD solver based on a finite volume formulation, was developed to solve the full Navier-stokes equations in orthogonal curvilinear form. The numerical study is conducted for a flow over a NACA0012 airfoil operating at a low Reynolds number. Velocity profiles, skin friction distribution and flow pattern, for different angles of attack, are plotted in order to determine the position and the size of the separated region. The aerodynamic coefficients are then evaluated to examine the separation effect on the airfoil performance. The control of the separation is investigated using a parabolic distribution blowing along the separated region. The benefits of the control process is viewed through the flow structure and the aerodynamic performances compared with the uncontrolled case.

2. NUMERICAL METHOD

2.1. Governing equations

The flow is assumed two-dimensional, unsteady, incompressible and viscous. Since the Reynolds number investigated is very low, a fully laminar flow along the airfoil is considered. The governing equations are transformed into an orthogonal curvilinear coordinate system (ξ,η), such that the coordinates are aligned to the airfoil surface. The following are the non-dimensional equations expressing the mass and momentum conservation [19]:

Continuity equation

$$\frac{1}{h_1 h_2}\frac{\partial}{\partial \xi}\left(h_2 V_\xi\right)+\frac{1}{h_1 h_2}\frac{\partial}{\partial \eta}\left(h_1 V_\eta\right)=0 \tag{1}$$

Momentum equation in ξ direction

$$\begin{aligned}
&\frac{\partial V_\varepsilon}{\partial t}+\frac{1}{h_1 h_2}\frac{\partial}{\partial \varepsilon}\left(h_2 V_\varepsilon V_\varepsilon\right)+\frac{1}{h_1 h_2}\frac{\partial}{\partial \eta}\left(h_1 V_\varepsilon V_\eta\right)= \\
&-\frac{1}{h_1}\frac{\partial p}{\partial \varepsilon}+\frac{1}{Re\, h_2^2}\frac{\partial}{\partial \eta}\left(\frac{V_\varepsilon}{h_1}\right)\frac{\partial h_1}{\partial \eta}-\frac{2}{Re\, h_1 h_2^2}\frac{\partial V_\eta}{\partial \eta}\frac{\partial h_2}{\partial \varepsilon} \\
&+\frac{2}{Re\, h_1 h_2}\frac{\partial}{\partial \varepsilon}\left(\frac{h_2}{h_1}\frac{\partial V_\varepsilon}{\partial \varepsilon}\right)+\frac{1}{Re\, h_1 h_2}\frac{\partial}{\partial \eta}\left(\frac{h_1}{h_2}\frac{\partial V_\varepsilon}{\partial \eta}\right) \\
&+\frac{2}{Re\, h_1 h_2}\frac{\partial}{\partial \varepsilon}\left(\frac{V_\eta}{h_1}\frac{\partial h_1}{\partial \eta}\right)+\frac{1}{Re\, h_1 h_2}\frac{\partial}{\partial \eta}\left[h_2\frac{\partial}{\partial \varepsilon}\left(\frac{V_\eta}{h_2}\right)\right] \\
&-\frac{1}{Re\, h_1 h_2}\frac{\partial}{\partial \eta}\left(\frac{V_\varepsilon}{h_2}\frac{\partial h_1}{\partial \eta}\right)+\frac{1}{Re\, h_1^2}\frac{\partial}{\partial \varepsilon}\left(\frac{V_\eta}{h_2}\right)\frac{\partial h_1}{\partial \eta} \\
&-\frac{V_\varepsilon V_\eta}{h_1 h_2}\frac{\partial h_1}{\partial \eta}+\frac{V_\eta^2}{h_1 h_2}\frac{\partial h_2}{\partial \varepsilon}-\frac{2V_\varepsilon}{Re\, h_1^2 h_2^2}\left(\frac{\partial h_2}{\partial \varepsilon}\right)^2
\end{aligned} \tag{2}$$

Momentum equation in η direction

$$\frac{\partial V_\eta}{\partial t}+\frac{1}{h_1h_2}\frac{\partial}{\partial \varepsilon}\left(h_2 V_\varepsilon V_\eta\right)+\frac{1}{h_1h_2}\frac{\partial}{\partial \eta}\left(h_1 V_\eta V_\eta\right)=$$
$$-\frac{1}{h_2}\frac{\partial p}{\partial \eta}+\frac{1}{Re\,h_1^2}\frac{\partial}{\partial \varepsilon}\left(\frac{V_\eta}{h_2}\right)\frac{\partial h_2}{\partial \varepsilon}-\frac{2}{Re\,h_1^2h_2}\frac{\partial V_\varepsilon}{\partial \varepsilon}\frac{\partial h_1}{\partial \eta}$$
$$+\frac{1}{Re\,h_1h_2}\frac{\partial}{\partial \varepsilon}\left(\frac{h_2}{h_1}\frac{\partial V_\eta}{\partial \varepsilon}\right)+\frac{2}{Re\,h_1h_2}\frac{\partial}{\partial \eta}\left(\frac{h_1}{h_2}\frac{\partial V_\eta}{\partial \eta}\right)$$
$$+\frac{1}{Re\,h_1h_2}\frac{\partial}{\partial \varepsilon}\left[h_1\frac{\partial}{\partial \eta}\left(\frac{V_\varepsilon}{h_1}\right)\right]+\frac{2}{Re\,h_1h_2}\frac{\partial}{\partial \eta}\left(\frac{V_\varepsilon}{h_2}\frac{\partial h_2}{\partial \varepsilon}\right)$$
$$-\frac{1}{Re\,h_1h_2}\frac{\partial}{\partial \varepsilon}\left(\frac{V_\eta}{h_1}\frac{\partial h_2}{\partial \varepsilon}\right)+\frac{1}{Re\,h_2^2}\frac{\partial}{\partial \eta}\left(\frac{V_\varepsilon}{h_1}\right)\left(\frac{\partial h_2}{\partial \varepsilon}\right)$$
$$-\frac{V_\varepsilon V_\eta}{h_1h_2}\frac{\partial h_2}{\partial \varepsilon}+\frac{V_\varepsilon^2}{h_1h_2}\frac{\partial h_1}{\partial \eta}-\frac{2V_\eta}{Re\,h_1^2h_2^2}\left(\frac{\partial h_1}{\partial \eta}\right)^2 \qquad (3)$$

here h_1 and h_2 are the metric stretching factors:

$$h_1=\sqrt{\left(\frac{\partial x}{\partial \xi}\right)^2+\left(\frac{\partial y}{\partial \xi}\right)^2}\ ,h_2=\sqrt{\left(\frac{\partial x}{\partial \eta}\right)^2+\left(\frac{\partial y}{\partial \eta}\right)^2}$$

The physical velocities are related to the computational velocities by the following relations:

$$U=\frac{1}{h_1}\left(\frac{\partial x}{\partial \xi}\right)V_\xi+\frac{1}{h_2}\left(\frac{\partial x}{\partial \eta}\right)V_\eta$$
$$V=\frac{1}{h_1}\left(\frac{\partial y}{\partial \xi}\right)V_\xi+\frac{1}{h_2}\left(\frac{\partial y}{\partial \eta}\right)V_\eta$$

The no-slip and no-penetration boundary conditions are applied on the airfoil surface for the clean case (without control) . The blowing control is prescribed through wall-normal velocity on the surface of the airfoil at the separated region. The far-field boundary condition is applied at the outlet of the computational domain, so that the velocity at the boundary is equal to U_0.

2.2. Grid generation

Orthogonal conformal grid generation with an O-type topology is obtained by applying the Von Karman-Trefftz transformation [20]. Various grid resolutions are tested to ensure the grid independence of the flow solution. The total number of 33,000 cells is adopted, since the solution exhibits negligible change with farther increase in the number of nodes. The far-field boundary is located at a distance 20 times the chord length, away from the airfoil surface. The grids are clustered near the airfoil surface in the wall-normal direction to resolve the steep gradients within the boundary layer and to capture the physical phenomenon more accurately (Figure. 1).

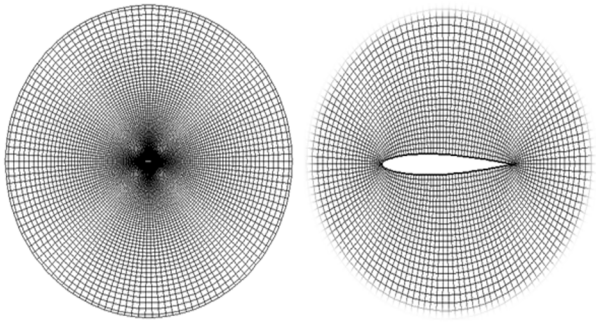

Figure 1. Structured grid around the airfoil

2.3. Numerical schemes

The discretization of the governing partial differential equations is based on the finite volume structured formulation [21-22]. The major advantage of the finite volume method is that the conservation laws are verified both locally on each finite volume and globally on the whole computational domain. The computational domain is decomposed into quadrilateral elements, the pressure is stored at the nodes and the two components of the velocity vector are stored at the cell faces in between the nodes. This way, the obtained staggered grid storage of the dependent variables, avoid the pressure field oscillations. A second-order accurate Adam-Bashforth scheme is applied for the time integration and a second-order accurate central difference scheme is applied for the convective terms discretization. The SIMPLER algorithm coupled with a staggered storage of the dependent variables, is used in order to handle the lake of a proper pressure equation. The resulting algebraic equations system is solved using the cyclic Thomas algorithm [23].

3. RESULTS

The code program implemented in fortran-90 language, includes six modules and performs calculations in double precision format. The program is developed to solve the 2-D, time dependent, laminar and incompressible Navier-Stokes equations in orthogonal curvilinear coordinates and can be applied to bodies of complex geometry shapes, to compute the flow characteristics and the aerodynamic coefficients.

3.1. Code validation

The solver is tested for the case of a flow about a circular cylinder to predict the boundary layer separation for a Reynolds number Re=1000. At a dimensionless time τ corresponding to 500 000 time steps, two separation cells appear at the back of the cylinder (Fig. 2).

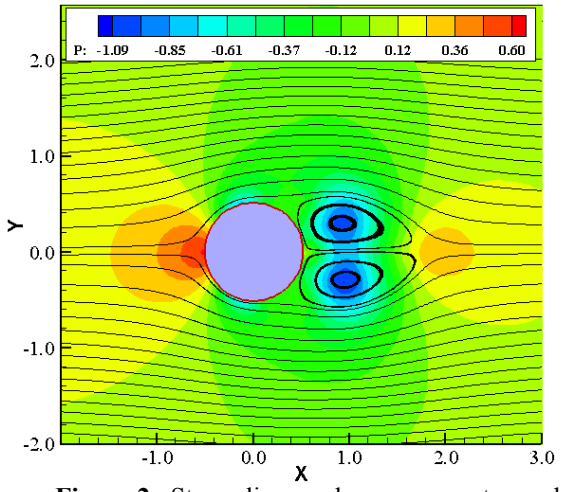

Figure 2. Streamlines and pressure contours about a circular cylinder for Re=1000

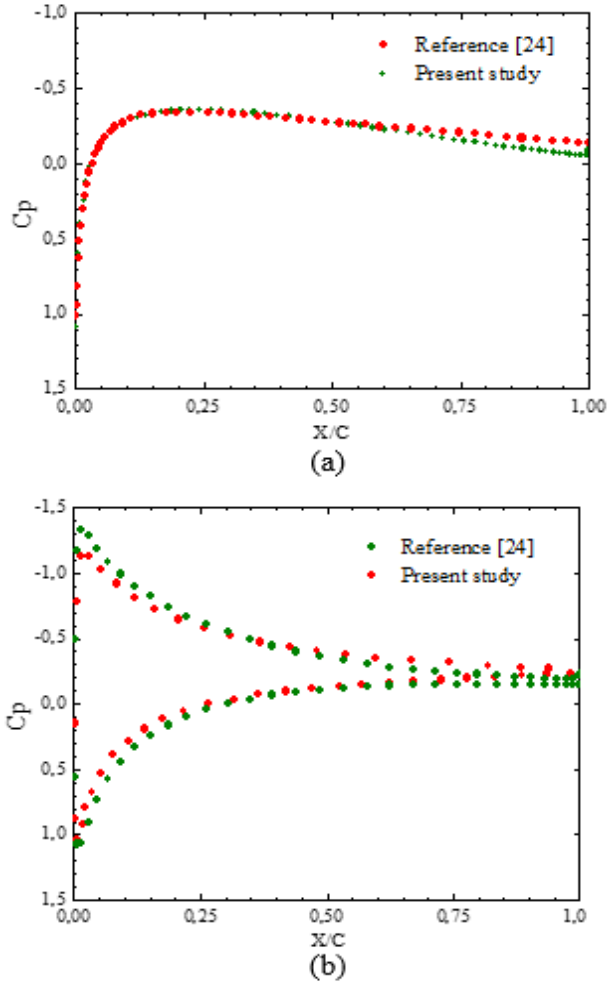

Figure 3. Cp distribution over NACA0012 for Re=500: (a) α=0°, (b) α=10°

A second validation of the solver is performed by applying it to compute the pressure coefficient distribution along a NACA0012 airfoil at a Reynolds number of 500, for two different angles of attack of 0° and 10°. The present simulations are compared with those obtained by Hafez et al. [24], for the same Reynolds number and the same angles of attack. Figure 3 illustrates the good agreement between the obtained results and those of the referenced study. It is worth noting that the maximum discrepancy is less than 5%, despite the different mathematical models used in the two studies. In the present study, the full Navier-Stokes equations are solved in the whole computational domain, while in the referenced study, the domain is divided to a viscous layer and an external potential layer.

The drag coefficient Cd predicted at a Reynolds number of 500 and an angle of attack of 0°, reported by Lockard et al. [25] is 0.1758 and the one predicted by Peng et al. [26] is 0.1760. These two results are in good agreement with the Cd obtained by the present study (Cd=0.1750).

3.2. Boundary layer separation

The main attention in this part of the study is paid to the location of the boundary layer separation point, the size and the strength of the separation bubble. The separation point is defined as the location where the wall shear stress is equal to zero with the apparition of an inflexion point on the velocity curve. The strength of the separation is defined as the ratio of the maximum reversed flow velocity to the mean flow velocity. The possibility of the reattachment of the separated layer is related to the amount of the momentum transferred to the separated region. If the amount of this momentum is sufficient to cause the necessary pressure rise to overcome the adverse pressure gradient, the reattachment will occur. At a relatively low Reynolds number, the transferred momentum may be insufficient to overcome the adverse pressure gradient and the separated layer may remain detached. These parameters of the separation are studied through the velocity profiles, the skin friction distribution and the streamlines distribution. First, velocity profiles as a function of the dimensionless wall-normal coordinates were computed in the boundary layer at three chordwise locations on the airfoil; x/c=0.6, 0.8 and 0.95 for the angles of attack between 0° and 15°. In Figure 4 the angle of attack is 8°, the velocity profile curve shows only an inflexion at x/c=0.95 chord length from the leading edge, indicating the separation point of the boundary layer. At 12°, as shown in Figure. 5, the strength of the separation is about 5% at x/c=0.8 and 10% at x/c=0.95. At 15°, shown in Figure 6, the strength of the separation is 5% at x/c=0.6, 10% at x/c=0.8 and almost 20% at x/c=0.95.

The location of the boundary layer separation can be also viewed from the distribution of the skin friction coefficient along the airfoil surface, for different angles of attack. The location of the separation point is defined by a zero skin friction coefficient. Figure 7 shows the skin friction distribution for different angles of attack. It can be seen from this latter figure that for 0° and 5° the skin friction is different from zero, showing that the separation does not occur. However, the skin friction on the suction side of the airfoil vanishes from x/c=0.85 at 8° of the angle of attack, x/c=0.65 at 10°, x/c=0.5 at 12° and x/c=0.3 at 15°, indicating that the separation point advances towards the leading edge as the angle of attack is raised.

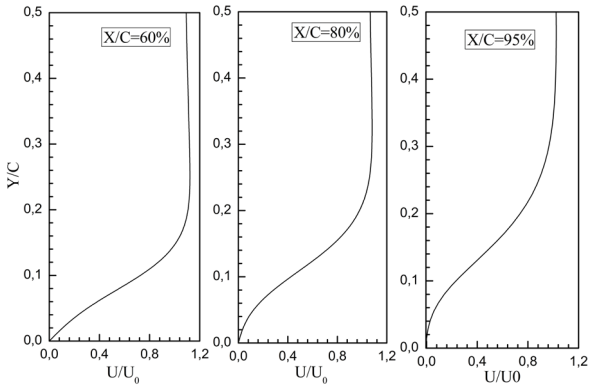

Figure 4. Velocity profiles at α=8°

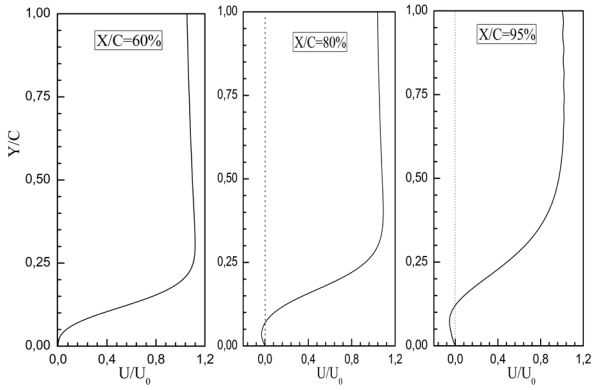

Figure 5. Velocity profiles at α=12°

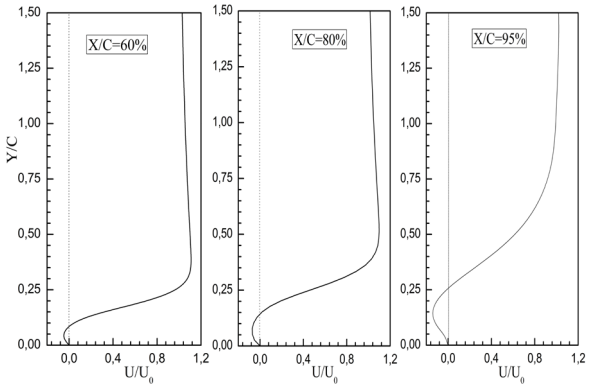

Figure 6. Velocity profiles at α=15°

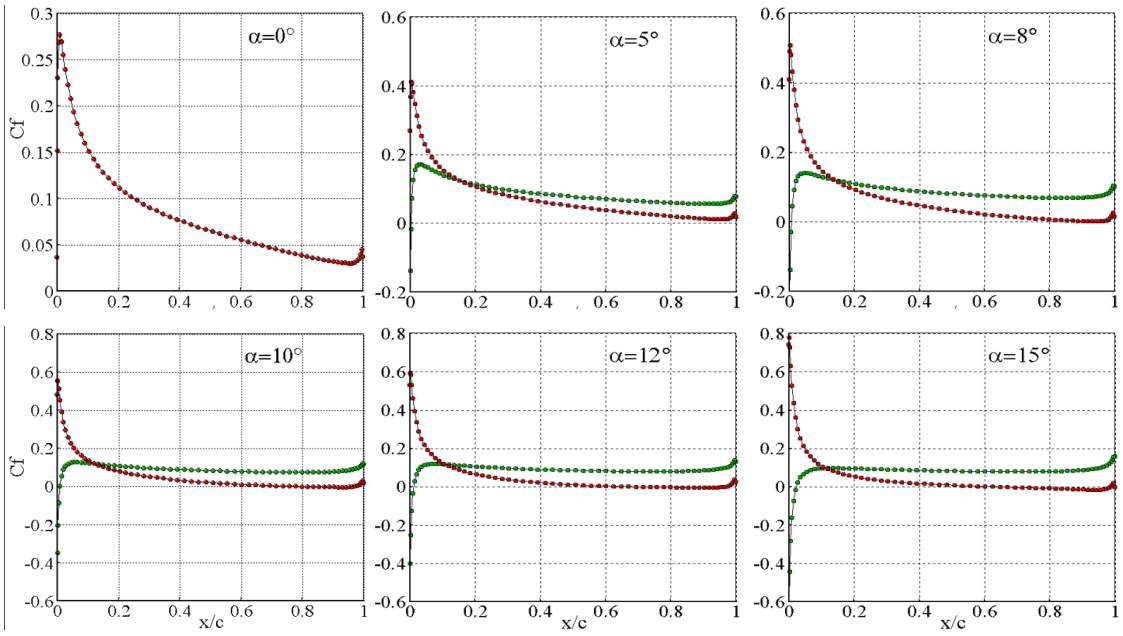

Figure 7. Skin friction coefficient distribution over a NACA0012 airfoil at Re=500, suction side (red), pressure side (green)

Streamlines distribution at different angles of attack gives a clear view of the minimum onset angle leading to separation and the evolution of the separated zone as the angle of attack is increasing (Fig. 8). At 8°, a small separation bubble appears near the trailing-edge of the airfoil. A further increase in the angle of attack causes an increase in the size of the separation bubble and the separation point moves towards the leading-edge. The location of the separation point for different angles of attack shown on the flow pattern is almost the same location predicted by the velocity profiles and the skin friction distribution.

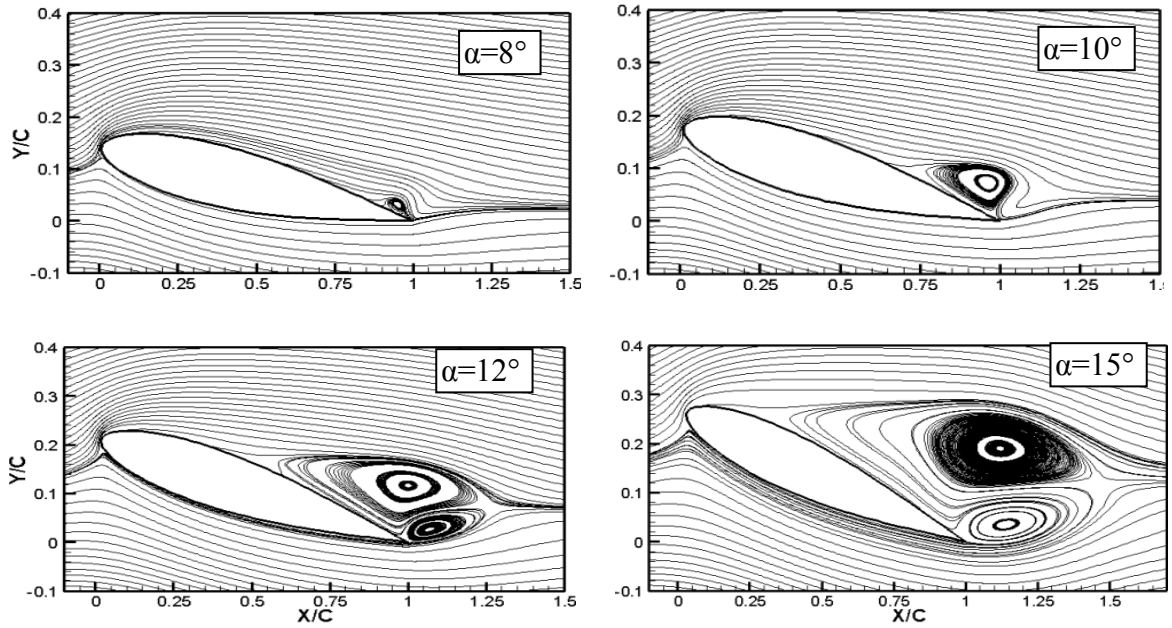

Figure 8. Streamlines representation about a NACA0012 airfoil at Re=500

3.3. Boundary layer separation control

The separated region investigated above is controlled using a parabolic distribution blowing. A tangential blowing is performed along the separated region. The blowing angle and position are chosen according to an earlier research published by Huang et al. [27]. The authors studied separately the suction and the blowing on a NACA0012 airfoil and concluded that the delay of the separation is more effective when a perpendicular suction is applied near the leading edge or a tangential blowing applied on the suction side of the airfoil. In the actual study, a parabolic distribution of the jet velocity ratio was opted in order to avoid the abrupt gradients velocity between the clean and the controlled surfaces. The graph illustrated in Figure 9a, shows the lift variations with the angle of attack without (baseline) and with blowing control for jet velocity ratio ranging from 0.1 to 0.3. The effect of the separation on the lift coefficient is presented by the baseline curve where the lift coefficient keeps increasing almost linearly up to the angle of attack of 8°. However, beyond α equal to 8°, a significant decrease in the slope of the lift curve can be seen, indicating the start of the boundary layer separation. The drop of the lift slope given by dCl/dα, has been estimated to be about 23%.

As the control is applied, a significant increase in the lift coefficient can be clearly seen. At an angle of attack α=12° and for a maximum blowing velocity ratio ϕ=0.3, a 22% increase in the lift coefficient is obtained.

The baseline curve shown in Figure 9b illustrates the loss in the lift to drag ratio, caused by the separation. The coefficient Cl/Cd increases rapidly before separation and slows down suddenly just beyond the onset separation angle α= 8°. The increase of the jet blowing velocity improves the maximum lift coefficient and affects moderately the drag coefficient, so the overall performances are improved with an increase of 7.55% in the lift to drag ratio reached for ϕ equal to 0.3 (Table 1). It was noticed that the higher the angles of attack, the more is the improvement of Cl/Cd.

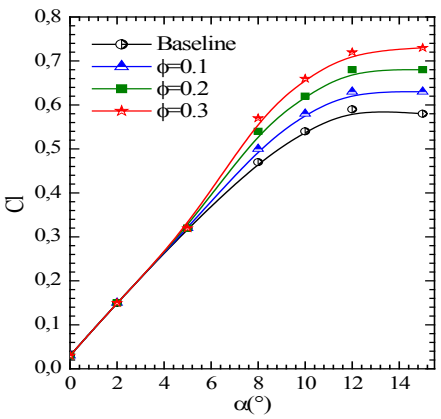

(a)

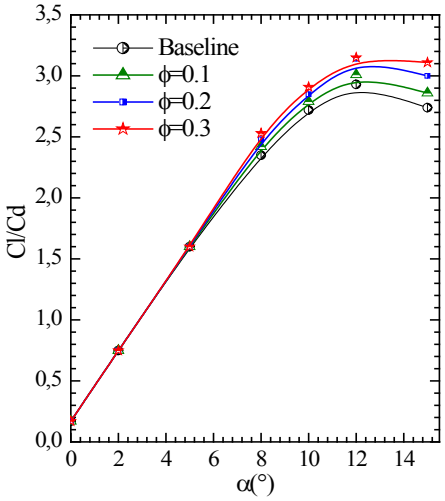

(b)

Figure 9. Effect of blowing control on NACA0012 aerodynamic performances

ϕ	*Cl*	*Cd*	*Cl/Cd*	*%Cl*	*%Cl/Cd*
0,0	0,59	0.20	2,93	---	---
0,1	0,63	0.21	3,01	7,58	2,78
0,2	0,68	0.22	3,14	15,50	7,19
0,3	0,72	0.23	3,15	21,87	7,55

Table 1: Dependence of the aerodynamic coefficients on velocity control at α=12°

The reverse flow obtained for different angles of attack at a location x/c=0.95 (Fig. 10), indicates that the effectiveness of the blowing control depends on the angle of attack and blowing velocity ratio. The higher the angle of attack the bigger the jet blowing ratio should be applied to eliminate the reverse flow. As it can be seen for α=15°, even for ϕ=0.3, the reverse flow is still present.

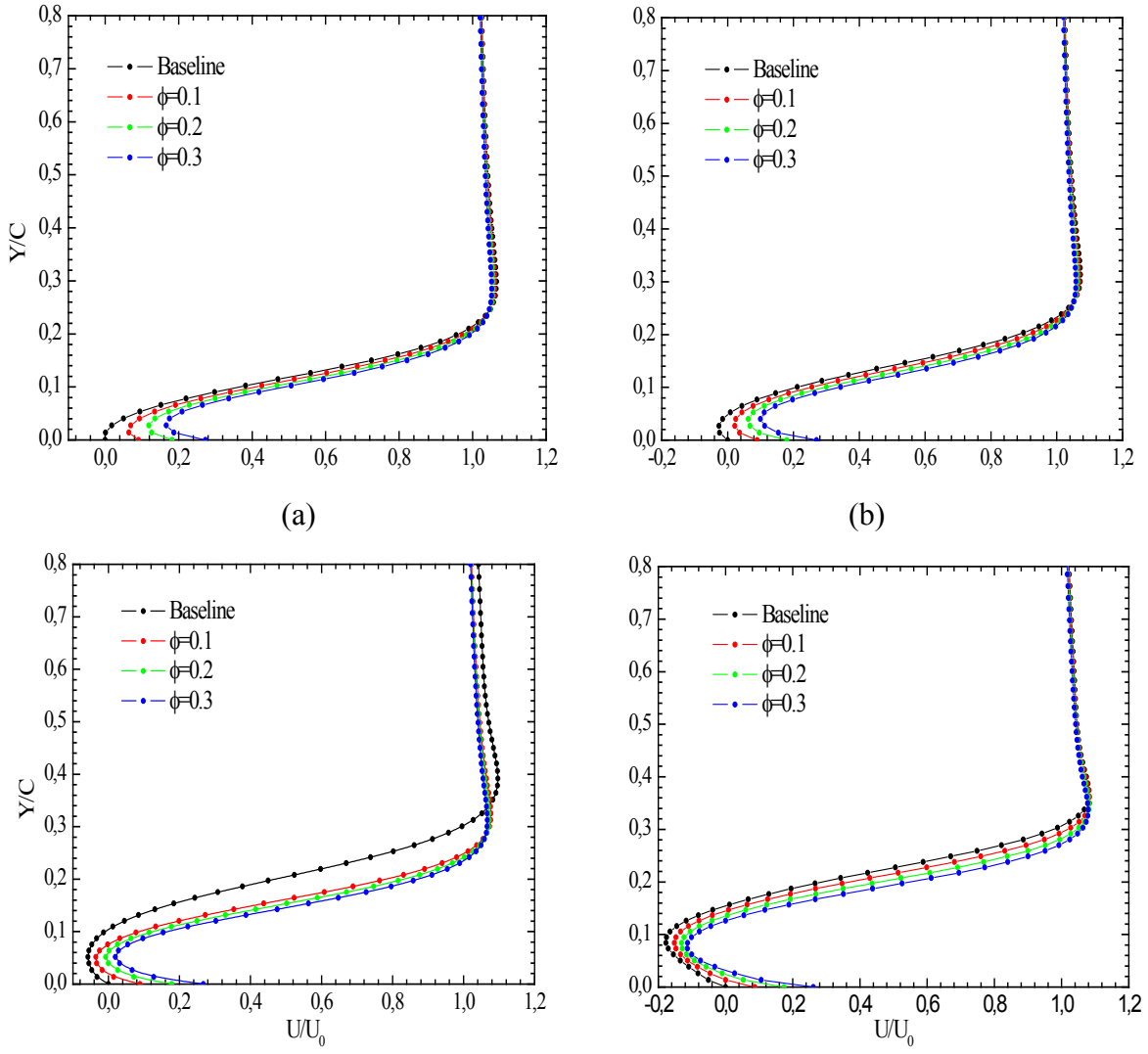

(a) (b) (c) (d)

Figure 10. Effect of blowing control on velocity profiles at different angles of attack: (a) α=8°, (b) α=10°, (c) α=12°, (d) α=15°

The control effect of the maximum velocity ratio on the flow structure for an angle of attack of 12°, is shown in figure 11. When the control process is applied with a blowing velocity ratio ϕ=0.1, the separation point initially located at 0.6 chord length from the leading edge, moves to 0.75 location with a significant reduction of the separation bubble size. As ϕ is increased to 0.2, the separation point goes more downward towards the trailing edge reaching the 0.85 chord length location. With a further increase of the blowing velocity up to 0.3 the separation bubble is completely suppressed.

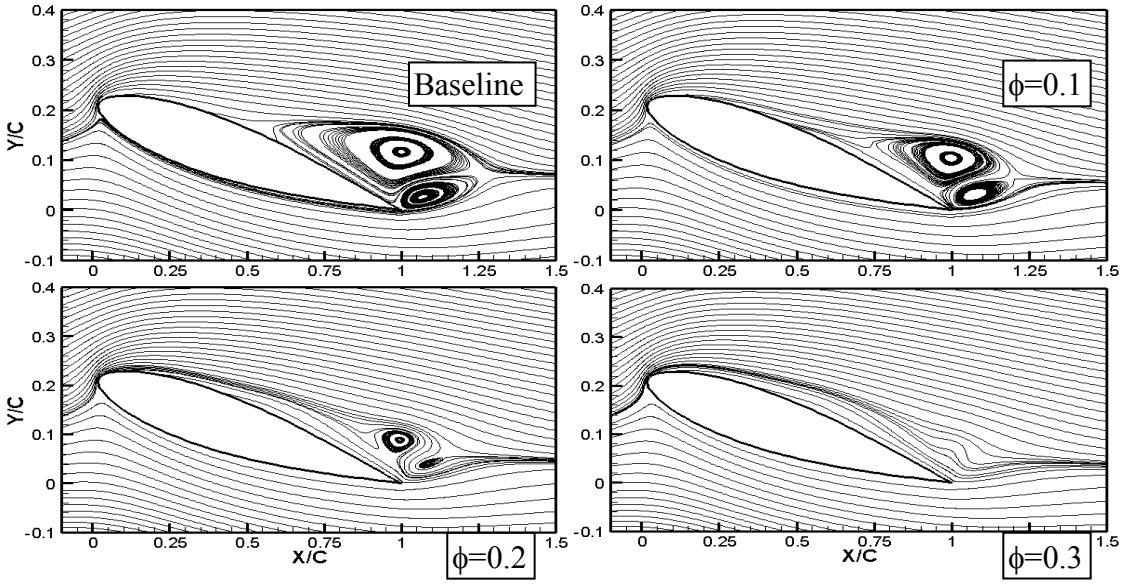

Figure 11. control velocity ratio effect on the separated region for an angle of attack α=12°

4. CONCLUSION

A numerical simulation has been carried out to study the separation of the boundary layer on a NACA0012 airfoil for a very low Reynolds number of 500. The computations were performed for different angles of attack. The finite volume method was used to discretize the incompressible full Navier-Stokes equations, written in curvilinear coordinates. For this purpose, a computer program has been developed. To handle the complexity of the airfoil geometry, a procedure for the orthogonal grid generation based on the conformal mapping, is combined to the solver. The accuracy of the developed solver has been tested for the case of the flow about a circular cylinder and in computing the pressure coefficient distribution along a NACA0012 airfoil. The solver makes it possible to predict the boundary layer separation through the velocity profiles, the skin friction distribution and the flow structure. It has been found that the separation zone begins to appear at an angle of attack of 8°. As the angle of attack increases the separated zone grows up and moves towards the leading-edge of the airfoil. It should be noted that the flow separation affects substantially the aerodynamic performances. The lift coefficient slope is reduced by about 23% and the lift to drag ratio slope is reduced by about 26%, just beyond the angle of attack at which the separation begins. The application of the boundary layer control concept using different tangential blowing velocities along the separation region, has demonstrated its effectiveness by delaying the separation bubble towards the trailing edge till its complete elimination for a blowing velocity ratio ϕ equal to 0.3. Thus, the overall aerodynamic performances have been improved by 22% in the maximum lift coefficient and by 7.5% in the lift to drag ratio.

REFERENCES

[1] S. Yarusevych, .J. G. Kawall, P. E. Sullivan, Separated-Shear-Layer development on an airfoil at low Reynolds numbers, AIAA Journal, 46 (2008) 3060-3069.

[2] W. Shyy et al, Computational aerodynamics of low Reynolds number plunging pitching and Flexible Wings for MAV Applications, 46th AIAA Aerospace science meeting and exhibit, January 7-10, 2008, Reo, NEVADA.

[3] Md. Mahbub, Y. Zhou, H. V. Yang, The ultra-low Reynolds number airfoil wake, Experimental Fluids, 48 (2010) 81-103.

[4] P. L. Delafin, F. Deniset, J. A. Asotolfi, Effect of the laminar separation bubble induced transition on the hydrodynamic performance of a hydrofoil, European Journal of mechanics B/Fluids, 46 (2014) 190-200.

[5] H. Shan, L Jiang, C. Liu, Direct numerical simulation of flow separation around a NACA0012 airfoil, Computers & Fluids, 34 (2005) 1096-1114.

[6] M. Alam, ND. Sandham, Direct numerical simulation of short laminar separation bubbles with turbulent reattachment, J. Fluid Mech, 410 (2000) 1-28.

[7] S. B. Hazra, A. Jamson, Aerodynamic shape optimization of airfoils in ultra-low Reynolds number flow using simultaneous pseudo-time stepping, Aerospace Computing Lab (ACL) report, 2007-4, 2007.

[8] W. Yuan, M. Khalid, J. Windte, U. Scholz, R. Radespiel, Computational and experimental investigations of low-Reynolds-number flows past an airfoil, The Aeronautical Journal, 111 (2007) 17-29.

[9] Y. Zhou, M. M. Alam, H. X. Yang, H. Guo, D. H. Wood, International Journal of Heat and fluid flow, 32 (2011) 329-339.

[10] S. Rajakumar, D. Ravindran, Computational fluid dynamics of wind turbine blade at various angles of attack and low Reynolds number, International Journal of Engineering Science and Technology, 2 (2010) 6474-6484.

[11] H. Shan, L. Jiang, C. Liu, M. Love, B. Maines, Numerical study of passive and active flow separation control over a NACA0012 airfoil, Computers & Fluids, 37 (2008) 975-992.

[12] K. Yousefi, S. R. Saleh, P. Zahedi, Numerical Study of flow separation control by tangential and perpendicular blowing on the NACA0012 airfoil, International Journal of Engineering, 7 (2013) 10-24.

[13] R. Wahidi, and D. Briges, Effects of distributed suction on an airfoil at low Reynolds number, AIAA Journal, 50 (2012) 523-539.

[14] Y. Hoarau, M. Braza, Y. Ventikos, D. Faghani, First stages of the transition to turbulence and control in the incompressible detached flow around a NACA0012 wing, International Journal of Heat and Fluid Flow, 27 (2006) 878-886.

[15] R. Azima, M. Hasana, M. Alib, Numerical investigation on the delay of boundary layer separation by suction for NACA 4412, Procedia Engineering, 105 (2015) 329-334.

[16] M. Serdar Genç, C. Kaynak, Control of laminar separation bubble over NACA2415 aerofoil at low Re transitional flow using blowing/suction, 13th International Conference on Aerospace Sciences & Aviation Technology, May 26-28, 2009, Cairo, Egypt.

[17] C. Brehm, A. Gross, H. F. Fasel, Open loop flow-control investigation for airfoils at low Reynolds numbers, AIAA Journal, 51 (2013) 1843-1860.

[18] L. Huang, P. G. Huang, R. P. LeBeau, Numerical study of blowing and suction control mechanism on NACA0012 airfoil, Journal of Aircraft, 41 (2004) 1005-1013.

[19] D. A. Anderson, J. C. Tannehill, R. H Pletcher, Computational Fluid Mechanics and Heat Transfer, Hemisphere Publishing Corporation, 1984.

[20] V. Kitsios, D. Rodriguez, V. Theofilis, A. Ooi, J. Soria, Journal of Computational Physics, 228 (2009) 7181-7196.

[21] S. V Patankar, Numerical heat transfer and fluid flow, Hemisphere Publishing Corporation, New York, 1980.

[22] S. Koshizuka, Y. Oka, S. Kondo, A staggered differencing technique on boundary curvilinear grids for incompressible flows along curvilinear or slant walls, Journal of Computational Mechanics, 7 (1990) 123-136.

[23] H. K. Versteeg, W. Malalasekera, An introduction to computational fluid dynamics: The finite volume method, Longman Group Ltd, Harlow, England, 1995.

[24] M. Hafez, A. Shatalov, E. Wahba, Numerical simulations of incompressible aerodynamic flows using viscous/inviscid interaction procedures, Comput. Methods Appl. Mech. Engrg., 195 (2006) 3110-3127.

[25] D. P. Lockard et al., Evaluation of PowerFlow for aerodynamic applications, Journal of statistical physics, 107 (2002) 423-478.

[26] Y. Peng et al., Application of multi-block approach in the immersed boundary-lattice Boltzmann method for viscous fluid flows, Journal of computational physics, 218 (2006) 460-478.

[27] L. Huang, R. P. LeBeau, P. G. Huang, Optimization of blowing and suction control on NACA 0012 airfoil using genetic algorithm, 42nd AIAA Aerospace Sciences Meeting and Exhibit, January 5-8, 2004, Reno, Nevada.

INVESTIGATION THE INFLUENCE OF ELECTRON BEAM PARAMETERS ON THE CATHODOLUMINESCENCE OF CADMIUM TELLURIDE.

Submited on 07/01/2018 – Accepted on 03/04/2018

Abstract

The cathodoluminescence signal (Cl) has been investigated theoretically for p-type CdTe, in order to understand the effect of incident electron beam parameters (energy Eo, intensity Ip), at low injection level, on the excess carriers, the cathodoluminescence intensity (ICl) and the depletion region (Zd). To do this a self-consistent calculation method of (ICl) has been used.

The obtained results show that the excess concentrations of carriers have a maximum value near the surface and decrease when E0 increases. Regarding the depletion region we observe a decrease of the depth as a function of Ip for the relatively great values and an increase with increasing Eo. The curves ICl = f(E0) show a maximum in the energy interval of [30-40 keV] and a rapid decrease for high values of Ip. Additionally, we observe, in general, an increase of ICl with increasing Ip. Finally, we record a linear variation of the intensity Cl as a function of Ip, according to different energies E0.

Keywords: *cathodoluminescence, CdTe, self-consistent method, depletion region, excess carriers, low injection level.*

D KENIECHE [1]
K GUERGOURI [2]

1 Laboratory of Physics and Chemistry of Semiconductors, Physics Department, Faculty of Exact Sciences, Frères Mentouri University Constantine, Algeria.

2 Faculty of Exact Sciences and Sciences of Nature and Life, University Larbi Ben M'Hidi, Oum El Bouaghi, Algeria.

I. INTRODUCTION

The cathodoluminescence phenomenon is a very effective means to study the surface and volume parameters of semiconductor materials [1-5].

Most theoretical studies of cathodoluminescence were performed on the III-V compounds, particularly GaAs [6-8]. In general, the method used is a self-consistent analysis, which gives a good agreement between calculations and experiment [8].

Although, several works have been done on the III-V materials, there are few investigations that have been carried out on the II-VI materials, despite their very interesting luminescence properties, particularly CdTe because of its direct gap and luminescence efficiency. That is why we are interested in the study of this material.

To do this we have used a generation function proposed by Wu and Wittry [9] using CdTe parameters [10]. In the previous work of the theoretical calculation of cathodoluminescence of CdTe ,we have reported the influence of surface and bulk parameters on the depletion region[11]

In this paper we investigated the influence of E_0 (energy of the incident beam) and I_p (intensity of primary electrons) on the excess carriers concentration, the depletion region developed at the surface of the semiconductor and the cathodoluminescence signal obtained after the interaction between electrons and material.

The calculation is based on the resolution of the continuity equation of both of the two type carriers in the neutral and depletion region.

2. BASES OF THE MODEL

∗ The studied material is: p type CdTe.

∗ The analytical shape of the dissipation function is that proposed by Wu and Wittry [9]; it is a modified Gaussian approximation.

∗ The study was performed using one dimension, the depth Z.

* The incident electron beam is perpendicular to the surface, which leads to a symmetrical resolution around incident beam axis.

∗ The penetration depth R_e of electrons is given by Kanaya and Okayama model [12].

∗ The surface carriers recombination is non-radiative.

* The occupation probability of any level is governed by Shockley-Read-Hall mechanism for the non-equilibrium conditions.

∗ The capture sections of electrons and holes are equal.

∗ The pseudo Fermi level is considered constant.

∗ The material is considered semi-infinite.

* In the depleted region, we assume that the recombination of excess carriers is negligible, while in the neutral region, the excess carriers have a stationary diffusion regime. The direct recombination of these carriers is at the origin of the cathodoluminescence phenomenon.

3. THEORETICAL CALCULATION OF Z_d AND I_{Cl}

3.1 Calculation of z_d

The absolute charge (Q) at the surface is given by [8]:

$$Q = e.Na.Z_d = e.N_t.(1-f) \quad (1)$$

Where e is the electron charge, Na the acceptor concentration, Nt the concentration of surface defects and f the occupation probability of the energy level of donors.
The depletion region width Zd is then deduced, it is given by:

$$Z_d = \frac{N_t(1-f)}{N_a} \quad (2)$$

The occupation probability f is given by the following expression:

$$f = \frac{\Delta n(0) + n_0 + n_i.\exp\left(\frac{E_i - E_t}{KT}\right)}{\Delta n(0) + n_0 + \Delta p(0) + p_0 + 2n_i.\cosh\left(\frac{E_t - E_i}{KT}\right)} \quad (3)$$

Where $\Delta n(0)$ and $\Delta p(0)$ are respectively the concentration excess of electrons and holes at the surface, n_i the intrinsic carrier concentration, n_o and p_o the electrons and holes concentrations at the surface respectively, E_i the intrinsic Fermi level and E_t the energy level in the band gap of surface defects.
In order to have $\Delta n(0)$ and $\Delta p(0)$ as a function of Z_d the continuity equation has been used. It is given by the following expression:

$$div.\vec{J} = G(z) - R(z) \quad (4)$$

Where $\vec{J}$ is the carrier flux, G(z) and R(z) are, respectively, the generation and recombination rates.
G(z) is expressed as a function of $\phi(u)$ by:

$$G(z) = \frac{\rho}{R_e}\phi(u) \quad (5)$$

Where ρ is the density of the semiconductor (in g/cm^3), R_e the penetration depth of electron (in g/cm^2) and $\phi(u)$ the dissipation function, expressed, according to Wu and Wittry [9] by:

$$\phi(u) = A.\exp\left[-\left(\frac{u - u_0}{\Delta u}\right)^2\right] - B\exp\left(-\frac{bu}{u_0}\right) \quad (6)$$

u is the normalized penetration ($u=\rho.Z/R_e$), Z being the depth.
u_0, Δu, A, B, b have been calculated by the authors, in a previous work, for CdTe [10], there are equal to:
Δu=0.17, u_0=0.057, b=3 and B/A=0.5
$\Delta n(0)$ and $\Delta p(0)$ are finally deduced and given by:

$$\Delta n(0) = \exp(\alpha.Z_d^2)[\theta_n - \xi_n erf(\sqrt{\alpha}.Z_d)] \quad (7)$$

$$\Delta p(0) = \exp(-\alpha.Z_d{}^2)[\theta_p - \xi_p F(\sqrt{\alpha}.Z_d)] \quad (8)$$

Where α is given by: $\alpha = \frac{e^2.N_a}{2.\varepsilon.KT}$ and θ_n,θ_p ,ξ_n,ξ_p are constants, obtained using the following boundary conditions:

$$\Delta n\left(Z_d^-\right) = \Delta n\left(Z_d^+\right)$$

$$\Delta p\left(Z_d^-\right) = \Delta p\left(Z_d^+\right)$$

$$\Delta n\left(Z_d^+\right) = \Delta p\left(Z_d^+\right)$$

$$J_n\left(Z_d^-\right) = J_n\left(Z_d^+\right)$$

$$\left.\frac{d\Delta n}{dz}\right|_{z=Z_d^-} = \left.\frac{d\Delta n}{dz}\right|_{z=Z_d^+}$$

To calculate Z_d we first introduce an initial value of Z_d in the transport equations for a given energy E_0 and intensity I_p. The resolution of these equations allows us to determine $\Delta n(0)$ and $\Delta p(0)$ and then to deduce a new value of Z_d. If the difference between the initial value of Z_d and the new one is weak, we take this latter as the value of Z_d. If, however, the difference is great we inject the new value in the program and run it again. We let's stop this process when the obtained Z_d is equal to the initial one.

3.2 Calculation of I_{Cl}

Only radiative processes in the neutral region are considered in the calculation of the cathodoluminescence intensity, which means that there are no recombinations in the depletion region, which allows the use of the low injection model. For a p type semiconductor, the I_{Cl} intensity is given by the formula:

$$I_{Cl} \approx \int_{Z_d}^{+\infty} \frac{\Delta n(z)}{\tau_r}\exp(-\alpha.z)dz \quad (9)$$

Where α is the absorption coefficient, and τ_r the radiative lifetime.
To obtain different values of I_{Cl} we calculate $\Delta n(z)$ and $\Delta p(z)$ related to final value of Z_d, calculated previously, and then I_{Cl} linked to (E_0, I_p) is calculated.

4. RESULTS AND DISCUSSION

4.1 Distribution of the excess carriers concentration:

The variation of the excess minority (electrons) and majority (holes) carriers concentration with the electron beam current are shown in Fig.1a and Fig.1b respectively. It is observed that these concentrations increase with the

increase in the beam current near the free surface, where the curves $\Delta n(0) = f(E_0)$ and $\Delta p(0) = f(E_0)$ show a maximum around E_0 = 15 keV. This is due to the strong generation carriers at low energies, on one hand, and on the recombination at high beam energies, on the other hand. Furthermore, it is observed that the excess concentration varies significantly with I_p, especially in the energy interval [10-20 keV] and there is no significant change for the high energy beam. This can be explained by the increase of the size of the generation volume, due to the electron penetration depths, which is deeper for the high energy beam.

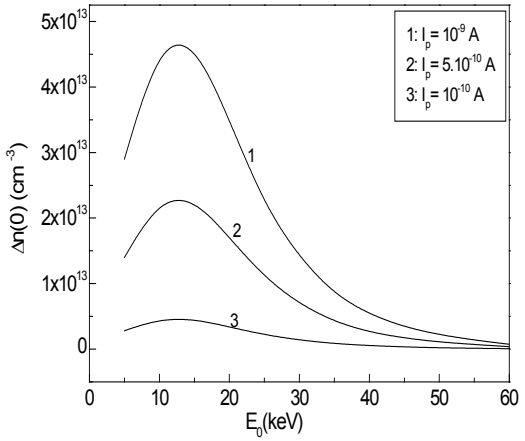

Figure 1a. Effect of the beam current on the minority carriers concentration - (E_t=1.4eV, L_n=1μm, N_t=10^8cm^{-2}, N_a=10^{15}cm^{-3})

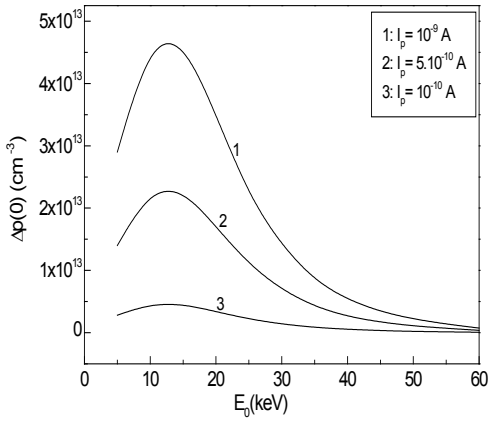

Figure 1b. Effect of the beam current on the majority carriers concentration - (E_t=1.4eV, L_n=1μm, N_t=10^8cm^{-2}, N_a=10^{15}cm^{-3})

4.2 The depletion region

To study the behavior of the depletion region width as a function of the beam excitation conditions (E_0, I_p), the surface and volume parameters are fixed; they are for CdTe: E_t = 1.4 eV, L_n = 1μm, N_t = 10^9cm^{-2}, N_a = 10^{15}cm^{-3}.

Figure 2 shows the variation of Z_d as a function of I_p for different values of E_0.

It is observed that Z_d remains constant for low values of I_p (I_p < 10^{-7}A) and starts to decrease after that. This is explained in terms of the concentration of excess carriers created by the excitation, which is low for low values of I_p. That's why we do not record any effect on Z_d. For higher intensities, the excess carrier concentration becomes high, which leads to an increase of the probability of occupancy of the surface states and hence a decrease of Z_d.

On the other hand, it is known that: when E_0 increases the depth of the electrons penetration increases at the same time, and leads therefore, to have a larger volume of generation, and thus a reduction of excess carriers at the surface. This leads to a decrease of Z_d.

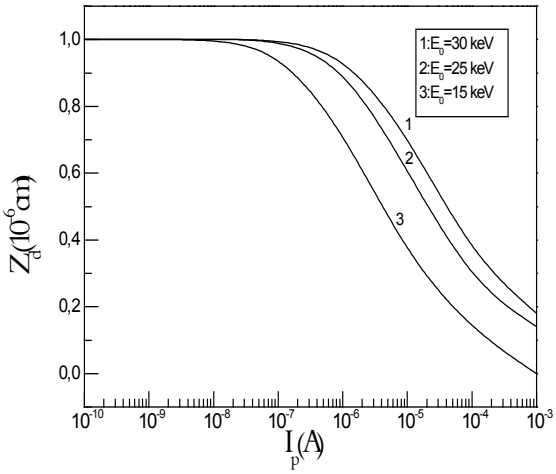

Figure 2. Influence of incident energy on the depletion region width
(E_t=1.4eV, L_n=1μm, N_t=10^9cm^{-2}, N_a=10^{15}cm^{-3})

4.3 The CI intensity

The theoretical curves ($I_{CI} = f(E_0)$) have been used to determine, quantitatively, the surface and volume parameters. The effect of I_p on the curves ($I_{CI} = f(E_0)$) is shown on Fig. 3, where it is observed, for each value of I_p, that the curves have a maximum between 30 and 40 keV. After that, the intensity starts to decrease.

The theoretical curves $I_{CI} = f(E_0)$ have been used to determine the quantitative physical values of the volume and surface. Figure 3 shows the influence of the current intensity of the incident beam (I_P) on the $I_{CI} = f(E_0)$ curves, which exhibit, for all I_P values, that the I_{CI} intensity has a maximum in the range [30 - 40 keV] of the incident beam energy.

The low accelerating voltages are related, generally, to phenomena surface, which allows us to say that the increase of I_{CI} as a function of E_0 up to the maximum is logical. In this section of the curve, it is estimated that the

cathodoluminescence signal is exclusively related to surface recombinations.

Once the maximum is reached, it is the influence of the volume, through the optical absorption phenomenon, which occurs to drop I_{Cl}, we record a rapid decrease of I_{Cl} for relatively high values of I_p.

Figure 4 shows the influence of the energy of the incident beam on the curves I_{Cl}= f (I_p). It is observed that I_{Cl} varies linearly as a function of I_p. This is in good agreement with previous works; which give the expression $I_{Cl} \sim I_p^m$, with 1< m < 2, m depending on I_p and E_o. It indicates the low injection regime.

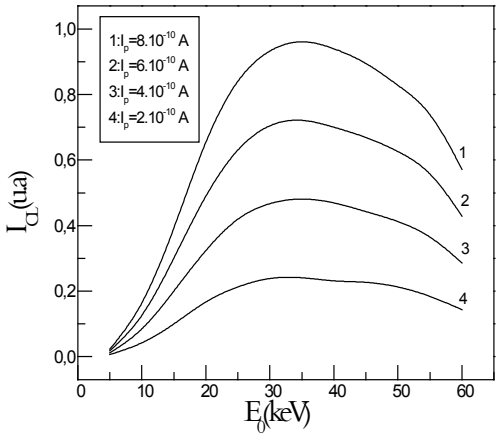

Figure 3. Variation of I_{Cl} intensity as a function of incident energy, for different current intensities
(L_n=1µm, E_t=1.3eV, N_t=10^8cm^{-2}, N_a=10^{15}cm^{-3}, α=10^4cm^{-1})

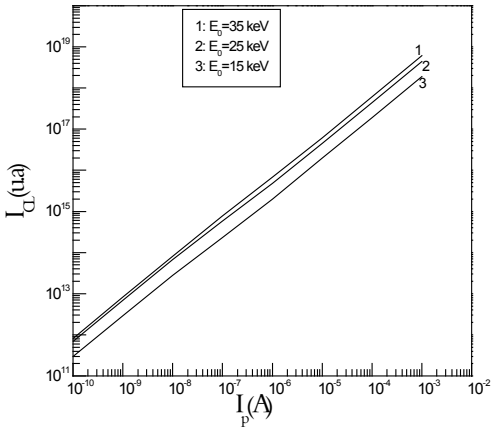

Figure 4. Variation of I_{Cl} intensity as a function of current intensity, for different energies
(Ln=1µm, E_t=1.3eV, N_t=10^8cm^{-2}, N_a=10^{15}cm^{-3}, α=10^4cm$^{-1)}$

5. CONCLUSION

In this study a theoretical investigation has been done to understand the effect of incident electron beam parameters (energy E_0, intensity I_p) on the excess carriers, the cathodoluminescence intensity (I_{Cl}) and the depletion region width (Z_d).
The influence of I_p on Δn(0) and Δp(0) is much greater for low values of the energy of the incident beam for large values.
On the other hand the calculation of the depletion region width (Z_d) and the cathodoluminescence intensity (I_{Cl}) as a function of electron beam parameters (E_0, I_p) indicates that Z_d remains constant for low values of I_p and decreases after that, and increases when E_0 takes great values. This analysis indicates also that the I_{Cl} = f(E_0) curves have a maximum in the range [30 – 40 keV] for different values of I_p. However we record a rapid decrease of I_{Cl} for large values of I_p. Finally, the calculation results in a linear variation of I_{Cl} with E_0 if the energy is below 35 keV.

REFERENCES

[1] S.Hildebrandt, J. Schreiber,W. Hergert, H. Uniewski and H.S. leipner, Theoretical fundamentals and experimental materials and defect studies using quantitative scanning electron microscopy cathodoluminescence/ electron beam induced current on compound semiconductors ,*Scann. Micr.*, 12, (1998), 535-552.

[2] J. Schreiber and S. Vasnyov,The dynamic mode of highresolution cathodoluminescence microscopy, *J. Phys.: Condens. Matter*, 16**,** (2004), S75-S84.

[3] Hui-fang Deng, and J. W. Steeds,Theoretical studies of minority carrier concentration profile and cathodoluminescence intensity in thin-film materials with different surface recombination velocities and constant excitation density, *Semicond. Sci.Technol.*, 7, (1992), 125-134.

[4] T. I. Kovtunuva, N.N. Mikheev, A. N. Polyakov, and M. A. Stepovich, On the possibility of the mathematical modeling of the dependence of cathodoluminescence intensity on the energy of beam electrons with the use of the power series approximation in the problem of identifying the parameters of semiconductor meterials, *J. Surf. Inv. X-ray, Sync. Neut. Tech.*, 4, (2010),778-783.

[5] F. Cléton, B. Sieber, R. A. Masut, L. Isnard, J. M. Bonard and J. D. Ganière, Photon recycling as the dominant process of luminescence generation in an electron beam excited n-InP epilayer grown on an n^+-InP substrate, *Semicond. Sci. Technol.*, 11, (1996), 726-734.

[6] W. Hergert, P. Reck, L. Pasemann, and J. Schreiber, Cathodoluminescence measurements using the scanning electron microscope for the determination of semiconductors parameters, *Phys. Stat. Sol. A*, 101, (1987), 611-618,.

[7] D. B. Wittry and D. F. Kyser, Surface recombination velocities and diffusion lengths in GaAs, *J. Phys. Soc. Japan Suppl.*, 21, (1966), 312-316.

[8] A. Djemel, R.J.Tarento, J. Castaing, Y. Marfaing and A. Nouiri, Study of electronic surface properties of GaAs in cathodoluminescence experiments, *Phys. Stat. Sol. A*, 168, (1998), 425-430.

[9] C. J. Wu, D.B. Wittry, Investigation of minority-carrier diffusion lengths by electron bombardment of schottky barriers, *J. Appl. Phys.*, 49, (1978), 2827-2836.

[10] D. Kenieche and K. Guergouri, Theoretical Investigation of the Effect of the Surface Parameters on Cathodoluminescence Signal, *J. Mat. Sci. Eng.*, 5, (2011), 473-477.

[11] D. Kenieche and K.Guergouri, Theoretical calculation of cathodoluminescence: Infuence of surface and bulk parameters on the depletion region of p-type CdTe, *Mod. Phys. Lett. B*, 30, (2016),1650057.

[12] K. Kanaya , S. Okayama, Penetration and energy-loss theory of electrons in solid targets, *J. Phys. D : Appl. Phys.*, 5, (1972), 43-58.

THE INFLUENCE OF THE VOIDS ON AN ADHESIVE LAP JOINT: EXPERIMENTAL AND NUMERICAL ANALYSIS.

Submited on 24/07/2017 – Accepted on 13/05/2018

Abstract

The aim of this paper is to present an experimental and numerical characterization, which is a typical adhesive for aerospace applications. This was done with two kinds of structures, with and without voids, and comparing their structural performance. Additionally, the X-RAY NONOTOM CT SCAN (computed tomography) has been used to determinate the distribution of the voids in the adhesive. Subsequently, numerical models, which represent experimental trials, were developed by modelling adhesives using the finite element technique. A shear test has been performed on the specimens in order to confirm the resistance of the bonded joint taking into account that the materials have the same mechanical characteristics. Then, the numerical simulation has been developed using the software ANSYS in order to analyze the adhesive lap joint model. The finite element displacement analysis of the single lap joint was examined for the cases with and without voids. The stress of the adhesive single-lap joints is mainly generated during the cooling process. The results between the experimental tests and the numerical model are in good agreement. In fact, it is noted that the numerical models have been shown to be very representative of experimental trials with reasonable maximum errors. Additionally, we have noted that the absence of the voids increase the stiffness of the lap joints with a reasonable percentage of the loads charges. In the absence of the voids, the load failure of the joint has been increased. However, the increase rate in the failure load changes depending on the structural features of the adhesive and the type of the adhesive.

Keywords: *Adhesive; lap joints; voids; deformation; load; adhesively bonded.*

F HADJEZ [1]
B NECIB [2]

Laboratory of Mechanical Engineering, Frères Mentouri University Constantine, Algeria.

I. INTRODUCTION

Adhesively bonded assemblies are increasingly used in the transport industries, such as automotive or aeronautics because of their numerous advantages: low-weight structure, high mechanical performance and relatively uniform repartition of stresses along the bonded area [1]. The fuselage of Boeing's 787 passenger aircraft is the large structures where composites are adhesively bonded with metals [2]. The first who develop an analytical model to determine the shear stress distribution in a single lap joint is Volkersen [5]. A modern technique developed in the product of the lap joint for the application [1, 2, 3, 4, 6] all of this modern technique is important for many engineering parts but it deferent to depending of the utilization, [2, 7, 11]. The airline industry has been marked by numerous incidents, in case of durable joints fibber reinforced composite materials widely used carp present extent strength and stiffness. For the aerospace application precisely the bonded joints, one of the main issues failure are the voids inside of the adhesive, we assumed that the voids are the original failure of the bonded joints under the big charges. These voids can be result from volatile impurities that evaporate when we assembling the lap joints during the curing process, another source of voids are the entrapment of the air between the adherend and the adhesive during manufacturing of joints [9].

The increasing of the shear stress at the end of the adhesive can be results of the presence of the voids [9, 8, 10]. Chadegani and Batra demonstrated that the effect of a void on the energy release rate of an interface crack [9, 11]. Ahmed Sengab and Ramesh Talreja reviewed a numerical study of failure of an adhesive joint influenced by a void in the adhesive [9]. All of these studies are recently proving.

The aim of this study is to use the following steps which are the loud characterization using Shear Test, X-RAY CT scan NANOTOM machine to determinate the existence and the distribution of the voids, and the software ANSYS numerical part resumes a simplified creating and control of the voids, like the precedents researches proving and confirming the existence of the voids, however, our hypotheses supposed that the original of the cracks results of the voids.

As consequence, the static analysis of a bonded joint is considered a non-linear analysis where the non-linearity is due to the presence of contacts and to different materials. This non-linearity of geometric type and material type is translated as the inability to solve the problem with a single step, therefore, arises the need to discretize the application of the displacement, by performing the simulation as a succession of simulations, each of which sees the final result of the previous simulation as the start condition.

2. REALIZATION OF THE SAMPLES:

Six samples are investigated these made of 56 mm thickness and 101.6 mm long, 25.4 mm wide composite plates. The overlap zone is 25, 4 mm^2 of surface us know in figure (1). The structural of the adhesive is epoxy DGEBA/EPONE/ F28, CAT/IPDA Isophrine Diamin. Used for assembling the two composite plates, the composite plates layer with 0, 02 mm of thickness.

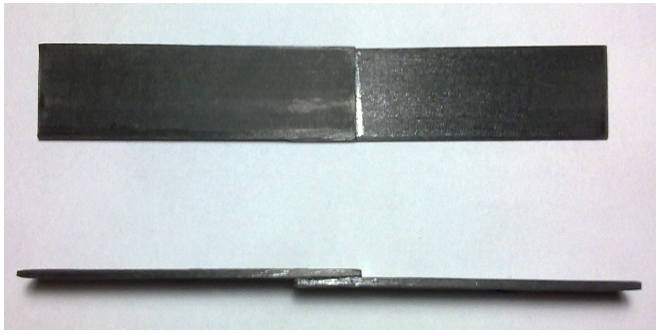

Figure 1: images of the samples

3. THE TEST OF THE SINGLE LAP SHEAR:

For the tests it was, first of all, estimated a maximum load value in order to choose a machine that will ensure the secure rupture of the specimens. Assuming that the average maximum shear stress was 40 MPA3, considering a contact surface of 645 mm2, we get a load of about 26 KN. Therefore we have chosen a machine of brand INSTRON Series 59804 with a floor (Figure 2) with load cell of 50 KN.

The clamping was entrusted to pneumatic jaws of 5 KN with flat grips in symbiosis with the typical normative geometries of the specimens for the mechanical testing of composite and elastomeric materials. In Figure 2 is shown a grabbed and ready for the test specimen.

The software for the acquisition of the data used to set various values, for both the output and the input, in order to generate a series of files that represent at the best the characterization of the mechanical properties regarding the experimental investigation. In general the most important parameters are:

* Load in N (ordinates)

The files generated by the software are:

* A report in pdf format representing the graph

* The machine management software files for further elaborations of data

* File.csv for Excel where there are the parameters ranked by columns.

However, for logistical reasons it was preferred to convert the data in file.txt and process them with Matlab. The tests were carried out by setting the most important parameters at the following values:

* Speed of the slide 2mm / min

* Sampling frequency of 10 hz.

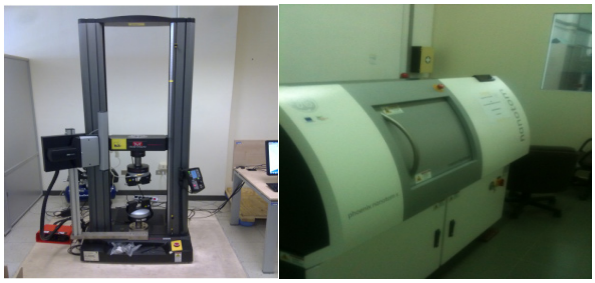

Figure 2: view of a X-ray nanotom machine and an INSTRON machine

4. THE EXPERIMENTAL RESULTS

At this point it is passed to the phase of execution of the tests carried out in two groups of 5 tests each. In figures 3 and 4 are the graphs of the load according to the displacement for each sample. the average values and the standard deviations of the most representative magnitudes of the mechanical properties of the bonded joint and that will be used later for the numerical model.

Using x-ray NANOTOM CT scan machine to analyzed the two samples. 3D view of the structure from the CT SCAN machine obtained (figure 5 And 6). A clear view of voids distribution, we can see a deferent distribution of voids apart from these manufacturing defects can also be identified using the x-ray CT scan. The study is almost half way through and some useful results have been obtained. Interesting numbers of micro voids are observed in addition some millimeters scan; according these results we can say that this subject has been further Clearfield.

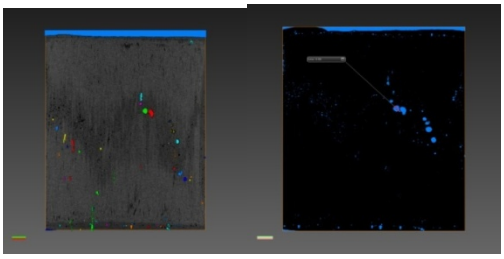

Figure 4: Joint Section Binary Image Slice CZM

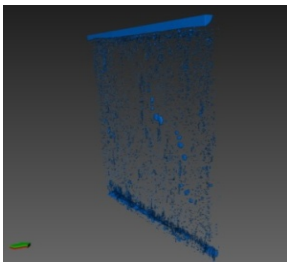

Figure 5: Joint Section Binary Image

The X-ray NANOTOM give us a deferent image when we could observed the voids in the adhesive, it can be of different shapes. It can be shown with a circular and in star forma. In the manufacturing process of adhesive joints, After the excel results by AVISO software with the image analysis we obtained in the section of CZM, when it was observed an interesting nembers of voids disturbed in the

surface of 490.3216 mm^3 under a big charge. These results make us doubting in the failures in the shear test.

Where is indicated with Fmed the maximum load, with δFmed the displacement corresponding to the maximum load, with τmed the average tangential tension at maximum load and with Etmed the total energy valued as area subtended by the load / displacement curve. The values were calculated excluding the experimental data that were mostly departed from their average values, and this, in order to evaluate the average properties avoiding the values characterized by great loss due to specific abnormalities which are not found on almost all of the samples.

The experimental data indicate the absolute improvement brought by the voids in terms of mechanical strength or for what concerns the toughness of the adhesive meatus (energy and maximum displacement). During the course of the test the gradual advance of the announced cracks was noted aurally by subsequent crackles. The final break instead happened with a dramatic crash and a cloud of smoke at the joint.

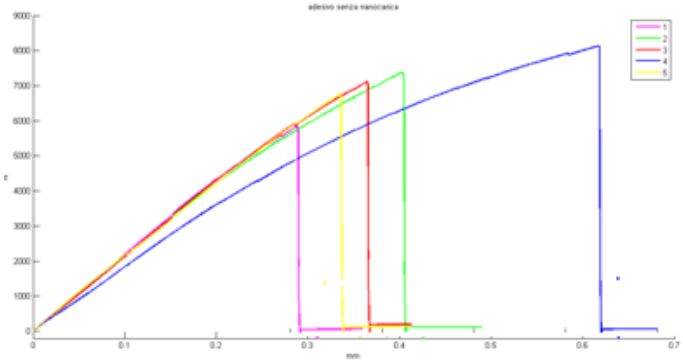

Figure 3: Results of the shear tests.

5. NUMERICAL SIMULATIONS

For the simulations we used the ANSYS WORKBENCH 15 software which constitutes a multi-physical simulation environment. It is an integrated platform, since the application packages that operate on simulations and other support software, are integrated with each other, that is, they have the ability to interact interchangeably; in practice it can easily pass, within the same working environment, from an application to another by transferring the database generated from a block to another, helped in this by a very versatile and advanced graphical interface typical of a structure of blocks

Here, has been used the Static Structural block for the static structural analysis while was used the ANSYS Composite PRE-POST packages for modelling of the adherents and the Mechanical Model environment for modelling of the adhesive film. It has been observed during the various iterations that by acting on the resin module of the bonding, it is acted also on the overall stiffness of the joint. With only the parameters of the models CZM it's not possible to set the stiffness of the adhesive film that affects the deformation at the break of the bonded joint. While the values of τ_{max} and critical ERR (ENERGY RELEASE RATE) govern the value of the breaking load. By iterating several times have been reached the values in Table 1 and which, remember, are related to a given configuration of the mesh and of the number of the total steps. With these parameters, were obtained the force-displacement features reposted in Figure 7a and 7b and Table 2 shows the main parameters and the errors compared to the experimental values of the joint. Note that increasing the displacement, the crack front, advances towards the central zone. This front is comparable to the area that goes from the blue areas to the red areas. However, for the evaluation of the crack front ANSYS WORKBENCH provides an output parameter defined as status, which is part of the contact Tool, whose purpose is precisely to plot the status of CZM contact.

A further advancement representation of the crack can be obtained observing the performance of the tangential tensions along the center line of the CZM contact, in function of the overlap abscissa and the load as a parameter. From Figure 7.a and 7.b it can be seen that increasing the load decreases the overlapping area after the de-cohesion of the contact. In particular in the transition from the represented status of tension, in the case without voids, from the purple curve to that of the red curve is shown the start of the structural crisis of the joint, and then the start of the path of the crack, which is characterized by the annulment of the shear stress at the ends of the overlapping area.

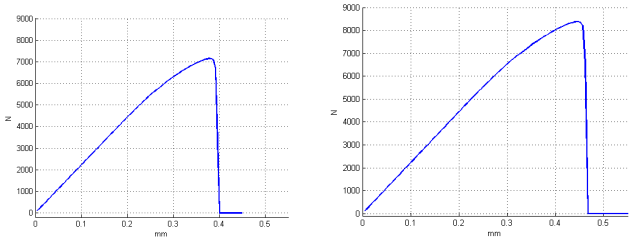

Figure 6.a: load-deformation

Adhesive-adhering relating to cohesive elements in the step in which the delaminating takes place of the joint. The increasing of the displacement, scrap towards the central zone. This resulted in comparable to the area that goes from blue to red areas. The advance of the front is not constant type straight line, along the width of the junction, but has a slight buckle. This is justified by noting that in the central area will have lower deformability of the joint related to further stress state that induce a more brittle behavior of the contact or an advance of breaking condition of CZM elements. Also note the increase of speed of crack propagation, with the advancement towards the central area of last cohesion. This is due to the intensification of tensions due to the increase of the load and decrease in the resistant surface. However, for the evaluation of the front crack in ANSYS Workbench provides an output parameter defined status, which is part of the Contact Tool, whose aim precisely to plot the status of CZM contact. In the figure 6.a and 6.d, and shows the status of the contact to the same step

of the tensions, the interface adhering-adhesive, in the figure 7.c and 7.d

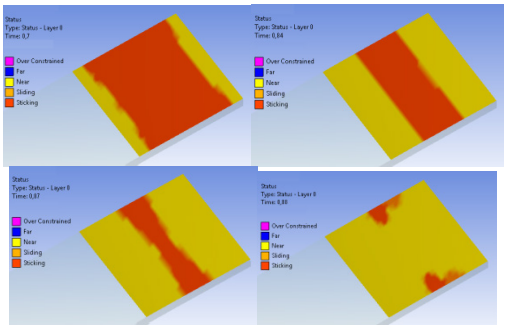

Figure 7.a: contact state by adhesive with voids

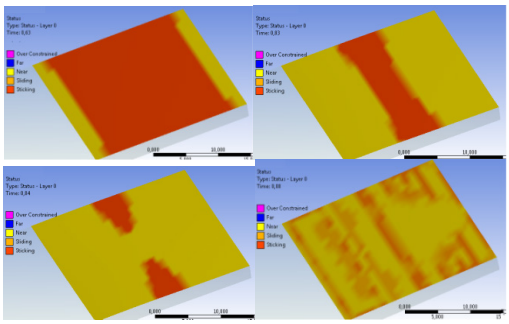

Figure 7.d: contact state by the adhesive without voids

DISCUSSION OF RESULTS:

This behavior is in line also with the slope of the force-displacement curve in which loses its linearity in correspondence with the above-mentioned load values. From the graphs of the τ of 8 a and 8 C figures, there is a certain similarity between the slopes of the curves of the first two lowest loads and the curves of the theoretical models (Figure 9) that help to validate the contact numerical model.

In 8.b and 8.d figures are plotted the curves τ (δ) obtained by APDL macro, where δ is the relative sliding between the Contact and Target surfaces chosen for creating the item CONTA174 used in the numerical model . These graphs while confirming the trend of the numerical theoretical models of debonding [3] allow to validate the simulations as it has been calculated, using always the same macro, the values of critical ERR comparing them with the values set in the cohesive model getting the results in table 4 Consider that the errors in the table are of computational type and discretization type.

This value 336,6 Mpa/mm decreasing the Young's modulus of the resin constituting the adhesive film, from 230 MPa to 260 MPa, we obtain the constitutive relationship which is characterized by: Kt = 34,64 GPa /mm (contact stiffness) which is about one order of magnitude less. Therefore it can be inferred, also observing the force-displacement, that too rigid film anticipates and accelerates the damage of cohesive elements inducing a more rigid behavior, more fragile and less resilient. Finally in Figures 8.g and 8.k reported the comparison between the experimental characteristics and those obtained with the simulations from which you also rely on the quantitative validation of the numerical model.

In the figures 8E and 8F, is reported the comparison between the experimental curves and those obtained with the simulations which indicate the qualitative validation of the numerical model.

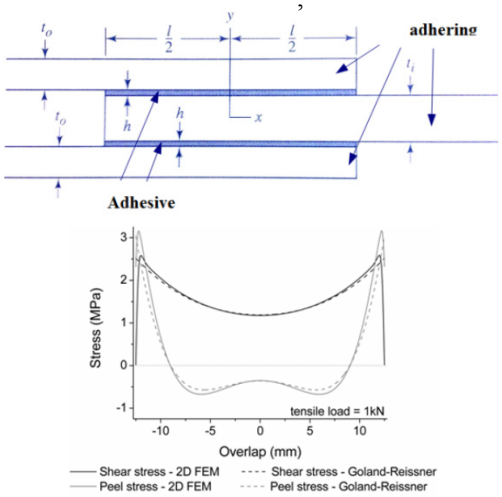

Figure 9: Comparison between the Goland Reissner theory and FEM

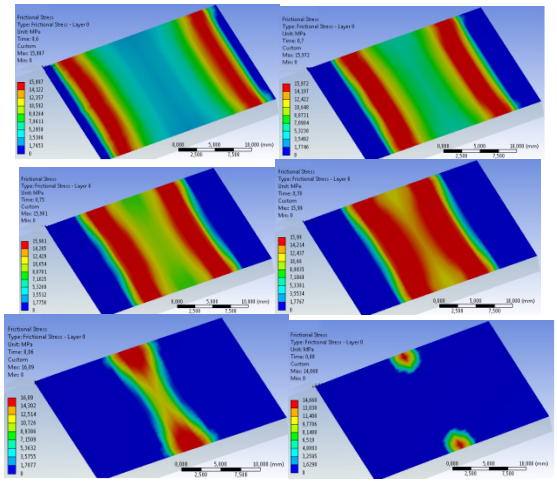

Figure 8.a: shear stress at the interface of the adhesive with voids

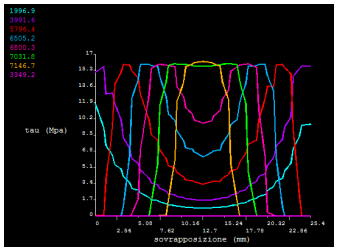

Figure 8.b: Shear stress at the centreline of the CZM contact at various values of the load (in N) for adhesive

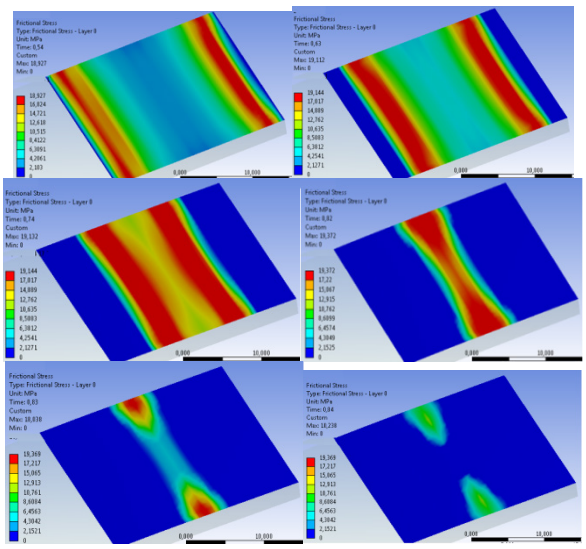

Figure 8.c: shear stress at the interface of the adhesive without

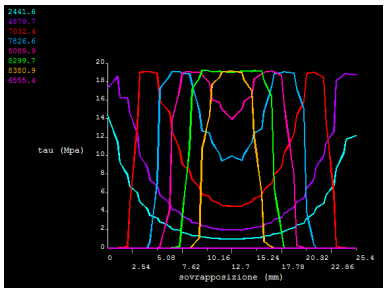

Figure 8.d: Shear stress at the centreline of the CZM contact at various values of the load (in N) for adhesiv

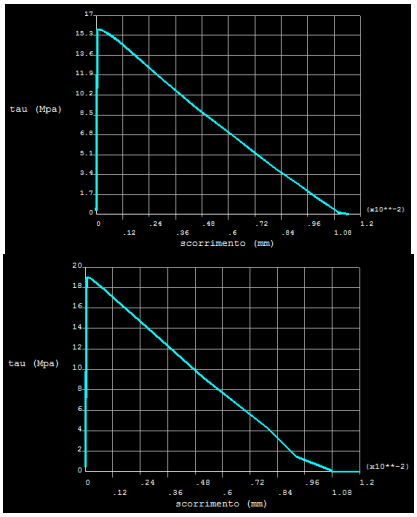

Figure 8.e and 8.f: constitutive relation the CZM model in the case of adhesive with and without voids

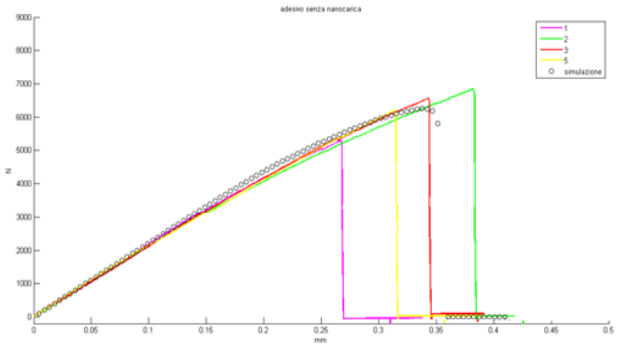

Figure 8.g: comparison between experimental and numerical data in the case with voids

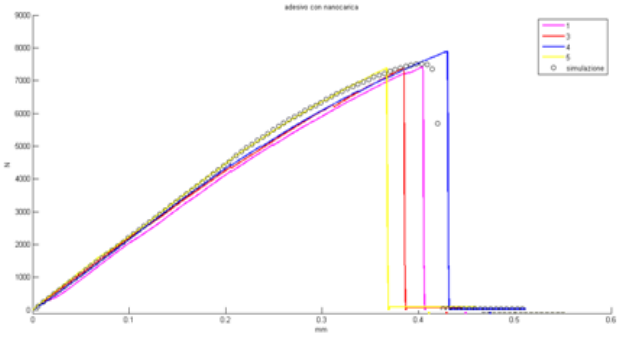

Figure 8.k: comparison between experimental and numerical data in the case without voids

6. CONCLUSIONS

In this study, the effects of voids on the adhesives, flexible and toughened adhesives at different tests on tensile failure load in single lap-joint geometry was investigated with an experimental and numerical analysis, the purpose of this, to improve and increase the mechanical performance and relatively uniform repartition of stresses along the bonded area, and decrease the weight structures, typical for adhesive aerospace applications, the results obtained were as follows:

- to improve and increase the mechanical performance and
- to distribute in a relatively uniform manner the stresses along the bonded area, and
- to decrease the weight structures, typical for adhesive aerospace applications, For the structural performance. Subsequently representative numerical models have been developed for modelling tests both the adherents that the adhesive using the technique of finite element. The main conclusions being reached and are as follows: Numerical models have shown well representative of the experimental tests with reasonable maximum errors. And after validation of the results the virtual cracks and the increasing of the shear stress cause the voids, considering the size of the voids because play a large role for the beginning of the expansion cracks in the adhesive, we couldn't confirm it experimentally, we must use another high technology machine under the control of the X-ray rayon, this technology simplified a direct view of the transformation of the voids, and the increasing of this cracks in the adhesive

with a 3D view of the deformation under big charge using the *3D metrology with high-resolution CT*.

REFERENCES:

[1] The transmission of Lamb waves across adhesively bonded lap joints to evaluate interfacial adhesive properties Emmanuel Siryabe, Mathieu Renier, Anissa Meziane, Michel Castaings Univ. Bordeaux, I2M, UMR 5295 CNRS, Bordeaux INP, F-33400, Talence, France

[2] Closed-form solutions for elastic stress–strain analysis in unbalanced adhesive single-lap joints considering adherend deformations and bond thickness Bo Zhao n, Zhen-HuaLu,Yi-NingLu

[3] A model for brittle failure in adhesive lap joints of arbitrary joint Configuration N. Stein, P. Weisgraeber, W. Becker

[4] Tomasz Sadowski , Przemysław Golewski, Marcin Knec Experimental investigation and numerical modelling of spot welding–adhesive joints response

[5] Zhu Y, Kedward K. Methods of analysis and failure predictions for adhesively bonded joints of uniform and variable bondline thickness: Office of Aviation Research, Federal AviationAdministration; 2005.

[6] Taguchi analysis of bonded composite single-lap joints using a combined interface–adhesive damage model D.C. O'Mahoney n, K.B.Katnam,N.P.O'Dowd,C.T.McCarthy,T.M.Young

[7] R.D.S.G. Campilho, M.F.S.F. de Moura, J.J.M.S. Domingues Numerical prediction on the tensile residual strength of repaired CFRP under different geometric changes

[8] Ye Zhang, Anastasios P. Vassilopoulos, Thomas KellerEnvironmental effects on fatigue behavior of adhesively-bonded pultruded structural joints

[9] Ahmed Sengab, Ramesh Talreja A numerical study of failure of an adhesive joint influenced by a void in the adhesive. Composite Structures (2016)

[10] Da Silva LF, Adams R, Gibbs M. Manufacture of adhesive joints and bulk specimens with high-temperature adhesives. Int J Adhes Adhes 2004

[11] Rossettos J, Lin P, Nayeb-Hashemi H. Comparison of the effects of debonds and voids in adhesive joints. J Eng Mater Technol 1994;116:533–8.